



# **First-principles Studies of Novel Two-dimensional Materials and Their Physical Properties**



**Yierpan Aierken**

Supervisor: Prof. François M. Peeters

Advisor: Dr. Ortwin Leenaerts

Dr. Deniz Çakır

Department of Physics, University of Antwerp

This dissertation is submitted for the degree of  
*Doctor of Philosophy*

Antwerp, Belgium

September 2017



*I would like to dedicate this thesis  
to my loving parents Arkin and Perwin,  
to my beloved wife Adila Dilshat,  
to my cherished sons Efran and Wildan.*



## **Declaration**

I hereby declare that except where specific reference is made to the work of others, the contents of this dissertation are original and have not been submitted in whole or in part for consideration for any other degree or qualification in this, or any other university. This dissertation is my own work and contains nothing which is the outcome of work done in collaboration with others, except as specified in the text and Acknowledgements. This dissertation contains fewer than 65,000 words including appendices, bibliography, footnotes, tables and equations and has fewer than 150 figures.

Yierpan Aierken  
September 2017



## **Acknowledgements**

And I would like to acknowledge ...



## **Abstract**

This is where you write your abstract ...



# Table of contents

<b>List of figures</b>	<b>xiii</b>
<b>List of tables</b>	<b>xvii</b>
<b>1 Results of Physical Properties Modification in Novel 2D materials</b>	<b>1</b>
1.1 Number of layers . . . . .	1
1.1.1 Few-layer of Calcium hydroxide . . . . .	1
1.1.2 Few-layer of pentasilicene . . . . .	16
1.2 Mechanical strain . . . . .	29
1.2.1 Carrier mobility enhancement in TiS <sub>3</sub> monolayer with strain	29
1.3 Heterostructures . . . . .	42
1.3.1 Electrical transport in 1T/2H/1T MoS <sub>2</sub> lateral heterostructure . . . . .	43
1.4 Defect induction . . . . .	51
1.4.1 Faceted blue phosphorene nanotube formed by line defects . . . . .	51
<b>Bibliography</b>	<b>63</b>
<b>List of Publications</b>	<b>73</b>



# List of figures

1.1	Atomic structure of bulk Ca(OH) <sub>2</sub> : (a) tilted view, (b) top view of one layer. . . . .	2
1.2	(a) Optical image of the crystal structure and (b) Raman spectrum measured using 488 nm laser in the low and the high frequency region. The fundamental phonon branches located at the low frequency (100-400 cm <sup>-1</sup> range) and the high frequency ( 3620 cm <sup>-1</sup> ) are associated with the OH stretching mode. (c) XRD measurements . . . . .	5
1.3	Different stacked bilayers (bottom layer is blurred) and their energy difference with respect to the AA stacking of Ca(OH) <sub>2</sub> , i.e. $\Delta E = E_{ABX} - E_{AA}$ , (X=1,2,...,5). Energies are given per formula of Ca(OH) <sub>2</sub> . Blue, green and red circles are for Ca atom, upper hydroxyl group and lower hydroxyl group, respectively. For clarity, the bottom layer is shifted slightly. . . . .	9
1.4	Interlayer interaction energy per formula of AA-stacked bilayer Ca(OH) <sub>2</sub> . Blue and red curves are for GGA calculations without and with vdW correction, respectively. . . . .	10
1.5	(a) and (d) are the Band structures, (b) and (e) are the partial DOS and (c) and (g) are the band and $k$ -point decomposed charge densities of the bulk (c) and monolayer (g) Ca(OH) <sub>2</sub> , respectively. The charge density are the band edges indicated in (a) and (d), isovalue are kept constant. (f) Band structure around $\Gamma$ point is shown with (dashed line) and without (solid line) spin orbit coupling. . . . .	13

1.6	Two lowest conduction band charge density of monolayer and bilayer Ca(OH) <sub>2</sub> at the $\Gamma$ point. . . . .	14
1.7	Phonon dispersion of monolayer Ca(OH) <sub>2</sub> . . . . .	15
1.8	(a) Side view and (b) top view of the atomic structure, (c) phonon spectrum and (d) two vibration modes with imaginary frequency of monolayer penta-silicene. Visualization of vibration modes is done with the V_Sim package [39]. . . . .	17
1.9	Schematic illustration of the four stacking types for bilayer p-Si. The colors of the symbols correspond to those of the monolayer in Fig. 1.8(a) and Fig. 1.8(b). The bottom layer in the bilayer is blurred for clarity. The arrow represents translation and the angle represents the rotation of the top layer with respect to the bottom layer. . . . .	18
1.10	Atomic structure of the $2 \times 2$ supercell of few-layer p-Si. The number of atomic layers in the bulk structure is fixed to four for comparison (i.e. $2 \times 2 \times 4$ and $2 \times 2 \times 2$ supercells for AA and AB <sub>r</sub> stacked bulk p-Si). (Visualisation using VESTA [42]). . . . .	20
1.11	Phonon spectra of different-stacked few-layer p-Si. . . . .	23
1.12	The cohesive energy of monolayer and AA and AB <sub>r</sub> <sup>d</sup> stacked bilayer p-Si as a function of time at a temperature of 100 K under NpT-ensemble. . . . .	24
1.13	Top and side views of the atomic structures of the $2 \times 2$ supercell of the three examined hexagonal silicene bilayers. . . . .	25
1.14	Electronic band structure of AA stacked few-layer and bulk p-Si, and a schematic of the first Brillouin zone. . . . .	26
1.15	Electronic band structures of AB <sub>r</sub> <sup>d</sup> stacked few-layer and AB <sub>r</sub> stacked bulk p-Si. The results for the monolayer are shown for comparison. . . . .	27
1.16	The charge distribution of CBM and VBM in AB <sub>r</sub> <sup>d</sup> stacked few-layer and AB <sub>r</sub> stacked bulk p-Si. The results for the monolayer are shown for comparison. . . . .	27
1.17	(a) Top and (b) tilted views of a $2 \times 2$ supercell of monolayer TiS <sub>3</sub> . Two crystallographic directions (where the strain is applied or the mobility is calculated) are shown with red and green arrows. . . . .	32

---

1.18 (a) The site and orbital-projected band structure (calculated using PBE functional) of the unstrained $\text{TiS}_3$ monolayer. Decomposed charge density of CMB (b) and VBM (c) at the $\Gamma$ point are presented. . . . .	33
1.19 Calculated elastic modulus along the $a$ and $b$ directions under mechanical strain. . . . .	35
1.20 Calculated phonon spectrum of (a) pristine monolayer $\text{TiS}_3$ and that under strain (b-g). . . . .	36
1.21 Variation of bond lengths with strain. Color of the curves matches with the color of the bonds in the structure depicted in the inset. . . . .	38
1.22 Variation of the band edges with respect to vacuum with strain. . . . .	39
1.23 Variation of the effective mass of electron and hole along the $a$ and $b$ directions at the $\Gamma$ -point with strain. . . . .	52
1.24 Variation of the (a) deformation potential constant ( $E_d$ ) with strain. . . . .	53
1.25 Variation of the mobility ( $\mu$ ) with strain. . . . .	54
1.26 (a) and (d) vertical and (c) and (d) lateral $\text{WS}_2/\text{MoS}_2$ heterostructures. Image adapted from: [101] . . . . .	55
1.27 Device models where 1H phase of $\text{MoS}_2$ is sandwiched between metallic $\text{MoS}_2$ electrodes. In (a) the $\alpha$ -device, (b) the $\beta$ -device, and (c) the $\gamma$ -device. For the $\alpha$ and $\beta$ devices, the interfaces between metallic and semiconducting $\text{MoS}_2$ have an armchair termination while a zigzag termination in the $\gamma$ -device. . . . .	56
1.28 The zero bias transmission spectra for (a) the $\alpha$ -device, (b) the $\beta$ device, and (c) the $\gamma$ -device. . . . .	57
1.29 Projected density of states of the valence and conduction band of 1H- $\text{MoS}_2$ as a function of electron concentration for the $\beta$ -device. Here, we only show the PDOS of the central part of 1H- $\text{MoS}_2$ where the effect of the interface is minimal. The Fermi level marks the zero energy. Electron concentrations (per formula unit of $1\text{T}_d$ phase) are given. . . . .	57
1.30 Variation of Schottky barrier for the $\beta$ -device as a function of electron concentration (per formula unit of $1\text{T}_d$ part) for both electrons (red) and holes (black). . . . .	58

1.31	Projected density of states of the valence and conduction band of the central part of 1H-MoS <sub>2</sub> for Re and Ta doped devices. In the top figure, gray region highlights the central part of 1H phase for which PDOS is calculated. For comparison, PDOS of bare device is also shown. . . . .	59
1.32	Projected density of states of 1H-MoS <sub>2</sub> at the different position on 1H-MoS <sub>2</sub> . The Fermi level marks the zero energy. . . . .	60
1.33	Self-consistent electrostatic potential profile along the interface of armchair (a) pristine and (b) doped 1T <sub>d</sub> -1H-1T <sub>d</sub> MoS <sub>2</sub> heterostructure. The right (left) 1T <sub>d</sub> MoS <sub>2</sub> is doped with Re (Ta). Blue curve denotes the plane average potential along the heterostructure. . . . .	61

# List of tables

1.1	Comparison of calculated results for structures parameter of bulk Ca(OH) <sub>2</sub> with experimental results and with theoretical results from other reference: lattice constants $a$ and $c$ , volume $V$ and $c/a$ ratio. . . . .	7
1.2	Calculated results for different structures of Ca(OH) <sub>2</sub> : lattice constants $a$ , vertical shift of O and H atom $c_O$ $c_H$ , Ca-O and O-H bond length, energy band gap $E_{gap}$ , cohesive energy per atom $E_{coh}$ , charge transfer from Ca atom to O atom $\Delta Q$ , in-plane Young's modulus $E_{xx}$ , $E_{yy}$ , in-plane Poisson's ratio $\nu_{xy}$ , in-plane shear modulus $G_{xy}$ and in-plane stiffness $C$ . For comparison, theoretical calculation on same quantities of BN are shown in the last row. . . . .	8
1.3	The cohesive energy ( $E_{coh}$ ), the interlayer binding distance ( $d_{inter}$ ), the interlayer binding energy ( $E_{inter}$ ), number of interlayer bonds ( $N_b$ ) and energy per bond ( $E_{bond}$ ) of the four possible stacking types of bilayer p-Si. The interlayer binding energy per unit cell is defined as $E_{inter} = E_{bi} - 2E_{mono}$ . . . . .	19
1.4	The layer (space) group for few-layer (bulk) systems. The lattice constant ( $a$ ), the interlayer distance ( $d_{inter}$ ), the nearest-neighbor bond length range ( $d_{min/max}$ ), the cohesive energy ( $E_{coh}$ ), and the band gap (PBE) of few-layer and bulk p-Si. . . . .	21
1.5	Mechanical properties of AB <sup>d</sup> bilayer p-Si . . . . .	24
1.6	The interlayer distance $d_{inter}$ , the nearest-neighbor bond length range ( $d_{min/max}$ ) and the cohesive energy per atom $E_{coh}$ of the most stable hexagonal bilayer silicene and bilayer p-Si. . . . .	26



# **Chapter 1**

## **Results of Physical Properties Modification in Novel 2D materials**

This is the second part of the results of this thesis. Here we will discuss some of the possible ways to modify the physical properties of 2D materials. As before, each section will be focused on an unique way to change the properties of materials, namely number of layers, mechanical strain, adatom adsorption, heterostructure and defect induction. In consist with the theme of the thesis, which is about novel 2D materials, we will continue to introduce other new 2D that has been discovered and whose properties will be modified. Some of the studies here are the continuum of the works in the previous chapter where properties are determined only, here those properties will be modified.

### **1.1 Number of layers**

#### **1.1.1 Few-layer of Calcium hydroxide<sup>1</sup>**

##### **Introduction**

We have seen several monolayer systems that exacted from layered materials such 2D-BN, 2D-MoS<sub>2</sub>, in this work, we further explore this process for alkaline earth metal hydroxides (AEMHs), which pose a layered structure in the bulk form. It was exfoliated to few-layer, the experiment and the theoretical modelling is

---

<sup>1</sup>This work is published in: P1.

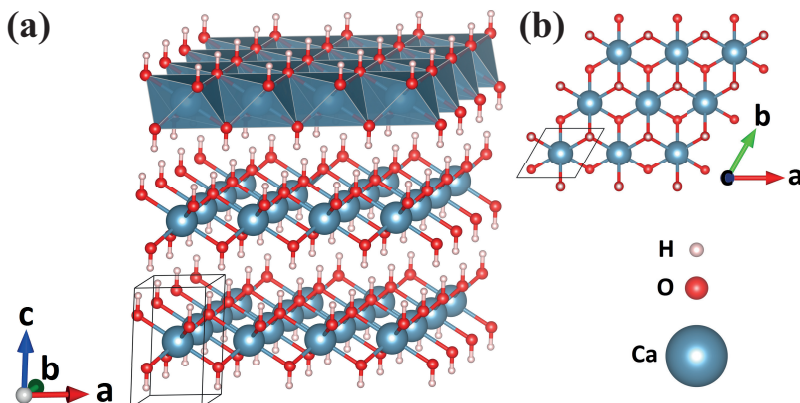


Fig. 1.1 Atomic structure of bulk  $\text{Ca}(\text{OH})_2$ : (a) tilted view, (b) top view of one layer.

reported in this section. In contrast to the abundant literature on graphenelike ultra-thin structures, few-layer AEMHs have not been investigated so far. Bulk forms of AEMHs are layered structures belonging to the  $P\bar{3}m1$  space group[1] and the crystal structure of a layered AEMHs comprises stacked sheets of  $\text{MO}_6$  ( $\text{M}$ =alkaline earth metals) edge-sharing octahedra, see Fig. 1.1. At each corner of an octahedron, each O atom binds one H atom and the latter interacts with three neighboring hydroxyl groups of the adjacent layer. Early studies on bulk AEMHs revealed that the application of temperature and pressure may result in dramatical changes in their crystal structure and their electronic properties[2-9]. Moreover, early theoretical studies showed the reliability of the use of first principle calculations with a plane-waves basis set in combination with the generalized gradient approximation exchange-correlation functional for the investigation of structural and electronic properties of these materials[10-13].

Although the structural and electronic properties of bulk AEMHs have been investigated before [12, 14, 15], single layers of these materials have never been studied before and their stability is still an open question. However, advances in experimental techniques made exfoliation and growth of such structures possible[16, 17]. Especially the Portlandite material,  $\text{Ca}(\text{OH})_2$ , which has been the main product of hydration of Portland cement,  $\text{CaO}$ , is one of the most well-known AEHMs, characteristic properties of ultra-thin structures of Portlandite have not been reported yet. In this study we investigate, both experimentally and theoretically, the structural, electronic, magnetic, vibrational and mechanical characteristics of bulk, bilayer and monolayer  $\text{Ca}(\text{OH})_2$  and discuss how these

properties change with the number of layers. Particularly, the result of the phonon calculation is presented for the confirmation of the stability of the newly proposed 2D material.

To assess the mechanical strength of the material, in addition to the elastic moduli that we have introduced in ??, here we calculate another useful parameter that closely related to the Young's modulus, which is called the in-plane stiffness of the materials. We focused on the harmonic range of the elastic deformation, where the structure responded linearly to strain  $\epsilon$ . The stretching of the  $\text{Ca(OH)}_2$  is achieved by increasing the equilibrium lattice constant  $a_0$  by  $\Delta a$ , to attain the axial strain  $\epsilon = \Delta a/a_0$ . We optimized the atomic structure at each increment of the strain,  $\Delta\epsilon = 0.01$  and calculated the total energy under strain  $E_T(\epsilon)$ . Then the strain energy can be given by,  $E_S = E_T(\epsilon) - E_T(\epsilon=0)$ ; namely, the total energy at a given strain  $\epsilon$  minus the total energy at zero strain. Then, using the following formula, one can calculate the in-plane stiffness:

$$C = \left( \frac{1}{A_0} \right) \left( \frac{d^2 E_S}{d\epsilon^2} \right), \quad (1.1)$$

where  $A_0$  is the equilibrium area of the supercell.

As explained in detail in the following sections, unitcells including one Ca, two O and two H are the primitive cells of both monolayer and bulk structures, it is doubled for bilayer. Cohesive energy per unit cell,  $E_{coh}$  is presented in table 1.2 and is calculated according to the formula:  $E_{coh} = E_{tot} - nE_{Ca} - 2nE_O - 2nE_H$ , where  $E_{tot}$  is the total energy of the unit cell of  $\text{Ca(OH)}_2$ ,  $E_X$  is the single atom total energy of atom X and  $n$  is the number of Ca atoms for the corresponding unit cell, i.e.  $n = 1$ ,  $n = 2$  and  $n = 1$  for monolayer, bilayer and bulk, respectively.

## Computational details

**Simulation program:** VASP and PHON[18]

**Energy cut-off:** 500 eV

**Pseudopotentials:** PBE-GGA(PAW)

**k points (Monkhorst-Pack):**  $35 \times 35 \times 1$  and  $25 \times 25 \times 11$  for few-layer and bulk  $\text{Ca(OH)}_2$ , respectively

**Vacuum:** 25 Å

**Energy and force convergence criterion:**  $10^{-5}$  eV and  $10^{-2}$  eV/Å, respectively

**vdW corrections:** DFT-D2 method of Grimme [19]

**Charge analysis:** Bader's charge analysis method[20-22]

## Experimental measurements

Before our theoretical investigation of few-layer Ca(OH)<sub>2</sub>, first we present the experimental realization and detailed theoretical analysis of the characteristics of bulk Ca(OH)<sub>2</sub> crystals.

Ca(OH)<sub>2</sub> crystals were grown using the hydrolysis technique by using Ca<sub>3</sub>SiO<sub>5</sub> micro-pallets. Ca<sub>3</sub>SiO<sub>5</sub> was mixed at different water to solid ratios ranging from 0.2 to 0.9 by molar weight. The mixture was heated up to 40 °C in a controlled reaction chamber for 3 hours and controllably cooled down to 5 °C for 24 hours using a temperature controller. The growth time depends on the total water to solid ratio as well as the growth temperature. Growth time was around 8 hours for 0.6 water to solid ratio and 40 °C growth temperature. Longer growth time typically resulted in a dendritic morphology where the growth was mostly in the c-axis direction. Synthesized crystals displayed rather sharp (FWHM 7 cm<sup>-1</sup>) Raman feature at 280 cm<sup>-1</sup> and our XRD measurements displayed sharp (00l) reflections at 19.1, 39, 56.2, 77.7 degrees implying that crystals have lamellar nature.

Synthesized crystals were around 0.1-2 mm in size and they were filtered from the solution. After the filtering process, crystallites were washed off using 18.2 MΩ.cm DI wafer multiple times and dried under inert Ar gas. Crystallites were exfoliated using micro-mechanical exfoliation technique onto thermal silicon oxide / Si substrates. We find that the contrast was improved for an oxide thickness around 265-285 nm. Exfoliated flakes displayed rather sharp edges (see Fig. 1.2) with well-defined angles of 120° and 60° implying that the materials are highly crystalline. Interestingly, synthesized Ca(OH)<sub>2</sub> flakes are layered in agreement with theoretical calculations and these flakes can be easily exfoliated using the Scotch tape technique on different substrates. The exfoliated flakes do not show any signs of structural imperfection, pit formation, and overall rather flat surfaces can be obtained. In Fig. 1.2, the yellowish looking regions actually correspond to regions where the thickness is around 50-100 nm (50-100 layers) while the blue features are only 10-50 nm in thickness. Considering the ease to exfoliate this material, experimentally and theoretically we predict that they can be eventually isolated down to mono- and few-layers on various substrates.

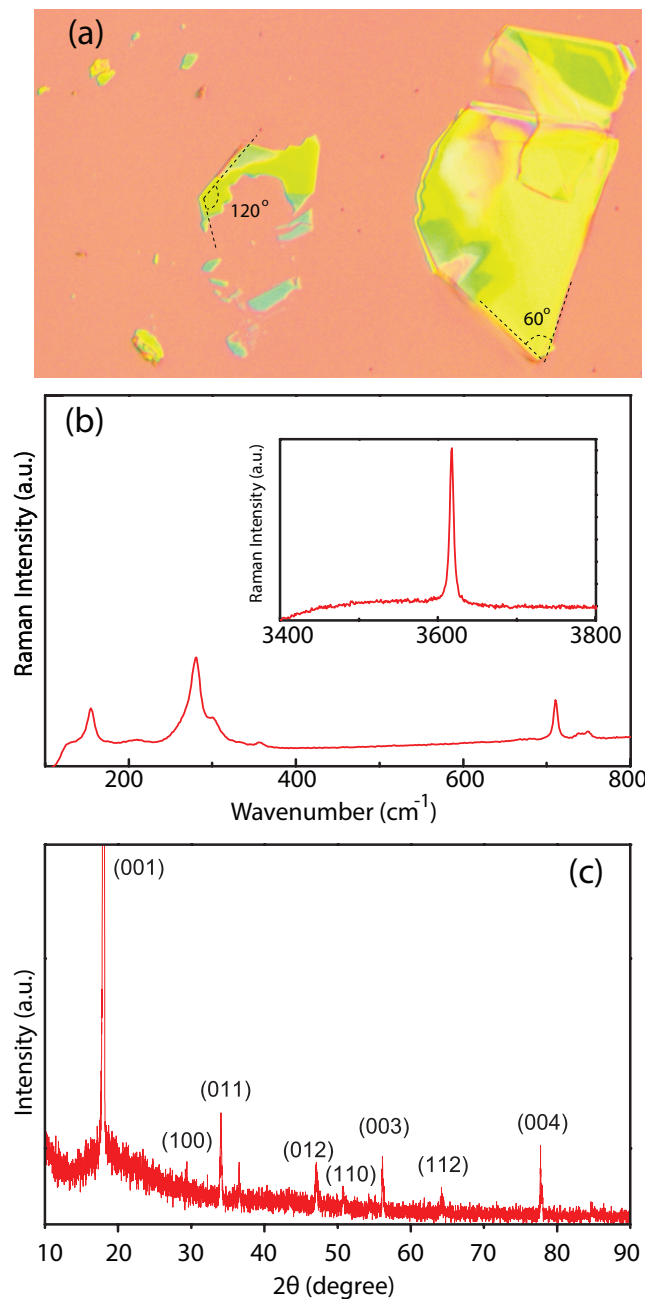


Fig. 1.2 (a) Optical image of the crystal structure and (b) Raman spectrum measured using 488 nm laser in the low and the high frequency region. The fundamental phonon branches located at the low frequency ( $100-400 \text{ cm}^{-1}$  range) and the high frequency ( $3620 \text{ cm}^{-1}$ ) are associated with the OH stretching mode. (c) XRD measurements

In addition, micro-Raman measurements were performed using a 488 nm laser on a 2 micron square spot using a high intensity laser of 10 mW. We noticed that few-layers of Ca(OH)<sub>2</sub> were not subject to local over-heating / decomposition effects unlike transition metal dichalcogenides (MoS<sub>2</sub>, WS<sub>2</sub>, etc.) which typically decompose around 100 microWatt power using a similar laser excitation spot. We attribute this to the low absorption of the material associated with the rather large band gap. Raman measurements displayed various peaks in the 100-1000 cm<sup>-1</sup> range. The high frequency peak at 3620 cm<sup>-1</sup> is associated with the O-H stretching mode  $A_{1g}$ . In addition, the low frequency  $E_u(T)$  mode is found at 280 cm<sup>-1</sup>.

Here, we note that even though this material is a direct gap semiconductor, their band gap is well beyond our detectors range and since the insulators cannot be excited with such high laser wavelength, PL measurements are virtually impossible.

### Structure properties

The bulk structure of Portlandite is formed by the stacking of individual Ca(OH)<sub>2</sub> monolayers on top of each other, see Fig. 1.1. As we will exam and discuss the stacking in detail in the following paragraphs, we learned that the AA stacking is the ground state atomic configuration for bulk and multilayer structures of Ca(OH)<sub>2</sub>. In table 1.1, optimized lattice parameters of the bulk structure together with experiments and other theoretical calculation are presented. Our results consist with reference [14] and together they have good agreement with experiments. This justify the reliability of our calculations.

In the 5-atomic hexagonal primitive unit cell of bulk Ca(OH)<sub>2</sub>, the Ca atom sits at the geometrical center of the cell, i.e. {1/2a, 1/2b, 1/2c}. Two O and two H atoms form two hydroxyl groups (-OH<sup>-</sup>) located symmetrically with respect to the Ca atom. In this arrangement, coordinates of H and O only differ by their positions along the **c** lattice axis and their fractional coordinates can be given as {1/6a, 1/6b, (1/2c - c<sub>O</sub>)} and {1/6a, 1/6b, (1/2c - c<sub>H</sub>)} for one hydroxyl, {5/6a, 5/6b, (1/2c + c<sub>O</sub>)} and {5/6a, 5/6b, (1/2c + c<sub>H</sub>)} for the other one, where c<sub>O</sub> and c<sub>H</sub> are the vertical shifts of the positions of O and H atoms from the Ca plane in the unit of Å , respectively.

Table 1.1 Comparison of calculated results for structures parameter of bulk  $\text{Ca}(\text{OH})_2$  with experimental results and with theoretical results from other reference: lattice constants  $a$  and  $c$ , volume  $V$  and  $c/a$  ratio.

Structure parameters	Exp. <sup>a</sup>	Exp. <sup>b</sup>	PBE-PAW (this work)	PBE-PAW <sup>c</sup>
$a$ ( $\text{\AA}$ )	3.589	3.592	3.614	3.612
$c$ ( $\text{\AA}$ )	4.911	4.906	4.982	4.942
$V$ ( $\text{\AA}^3$ )	54.78	54.82	56.35	55.85
$c/a$	1.368	1.366	1.379	1.368

<sup>a</sup> Ref. [23]

<sup>b</sup> Ref. [24]

<sup>c</sup> Ref. [14]

In the optimized structure, the lattice constants  $a$  and  $c$  are 3.61  $\text{\AA}$  and 4.98  $\text{\AA}$  in the bulk structure, parameters  $c_O$  and  $c_H$  are calculated to be 1.15  $\text{\AA}$  and 2.12  $\text{\AA}$ . Bond length of Ca-O and O-H are 2.36  $\text{\AA}$  and 0.97  $\text{\AA}$ . Interlayer distance which is defined as the distance between the uppermost H-layer of the underlying layer and the lowermost H-layer of the top-lying layer is found to be 0.49  $\text{\AA}$ . Differing from other lamellar bulk crystal structures such as graphite (3.58  $\text{\AA}$ ) and  $\text{MoS}_2$  (3.42  $\text{\AA}$ )[25] ,  $\text{Ca}(\text{OH})_2$  layers are more closely stacked on top of each other.

Our calculations revealed that going from bulk to monolayer the in-plane lattice parameter  $a$  change to 3.62  $\text{\AA}$  . In our calculations, the  $c$  lattice parameter in the hexagonal unit cell of the monolayer is set to 25  $\text{\AA}$  in order to avoid interlayer interaction between the adjacent layers. In the monolayer  $\text{Ca}(\text{OH})_2$ , parameters  $c_O$  and  $c_H$  are calculated to be  $c_O=1.14 \text{\AA}$  and  $c_H=2.10 \text{\AA}$  , respectively. Ca-O and O-H bond distances are 2.38  $\text{\AA}$  and 0.97  $\text{\AA}$  in the monolayer, respectively. We observed only quite small change as the system going from bulk to monolayer, some of the structure parameters even left unchanged, from this we can conclude quite weak interlayer interaction in  $\text{Ca}(\text{OH})_2$ . In order to study the interlayer interaction we further investigate their effect on stacking, and by including the vdW correction in the functional we are able to identify the nature of this interaction.

Individual layers of lamellar structures such as graphite, hex-BN and TMDs are held together mainly by the van der Waals force in order to form a bulk layered structure. Such a weak interaction stems from dynamical correlations

Table 1.2 Calculated results for different structures of  $\text{Ca(OH)}_2$ : lattice constants  $a$ , vertical shift of O and H atom  $c_O$   $c_H$ , Ca-O and O-H bond length, energy band gap  $E_{gap}$ , cohesive energy per atom  $E_{coh}$ , charge transfer from Ca atom to O atom  $\Delta Q$ , in-plane Young's modulus  $E_{xx}$ ,  $E_{yy}$ , in-plane Poisson's ratio  $\nu_{xy}$ , in-plane shear modulus  $G_{xy}$  and in-plane stiffness  $C$ . For comparison, theoretical calculation on same quantities of BN are shown in the last row.

	$a$ (Å)	$c_O/c_H$ (Å/Å)	Ca-O/O-H (Å/Å)	$E_{gap}$ (eV)	$E_{coh}$ (eV)	$\Delta Q$ (e)	$E_{xx}, E_{yy}$ (N/m)	$\nu_{xy}$	$G_{xy}$ (N/m)	$C$ (J/m <sup>2</sup> )
<b>Bulk <math>\text{Ca(OH)}_2</math></b>	3.61	1.15/2.12	2.36/0.97	4.08	4.52	1.6	55.0	0.30	21.23	60.1
<b>2L <math>\text{Ca(OH)}_2</math></b>	3.62	1.15/2.12	2.38/0.97	3.70	4.48	1.6	50.7	0.32	19.16	55.6
<b>1L <math>\text{Ca(OH)}_2</math></b>	3.62	1.14/2.11	2.38/0.97	3.67	4.39	1.6	50.7	0.33	19.08	53.2
<b>1L BN</b>	2.51 <sup>a</sup>	-	1.45 <sup>a,b</sup>	4.64 <sup>a</sup>	8.82 <sup>a</sup>	0.43 <sup>a,c</sup>	278.2 <sup>d</sup>	0.22 <sup>d</sup>	113.5 <sup>d</sup>	267 <sup>e</sup>

<sup>a</sup> Ref. [26]

<sup>b</sup> B-N bond length

<sup>c</sup> charge transfer from B to N

<sup>d</sup> Ref. [27]

<sup>e</sup> Ref. [28]

between fluctuating charge distributions in neighboring layers. Here we investigated the energies of various bilayer configurations. As presented in Fig. 1.3 there are six possible types of stacking between two  $\text{Ca(OH)}_2$  monolayers. Similar to the stacking nomenclature of bilayer graphene, we classify the stacking types to be either AA or ABn ( $n=1,2,\dots,5$ ). The same type of atoms from different monolayers are on top of each other in AA stacking whereas AB stackings can be reached by shifting one of the layers along certain lattice vectors. One set of AB stackings could be realized by shifting the second layer in the AA stacking towards  $[1\bar{1}0]$ , which gives stacking AB1, and by shifting towards the  $[110]$  direction, which gives stacking AB2, see first row in Fig. 1.3. Another set of bilayers are achieved by first flipping the second layer upside down in AA stacking, which would give stacking AB3, then AB4 and AB5 can be constructed by doing the same shifting on the second layer of AB3 towards  $[\bar{1}\bar{1}0]$  and  $[110]$  directions of the 1st layer, respectively. After relaxation of all stackings, the variation of the  $a$  lattice constant among the different stacking types is less than 0.01 Å. The smallest interlayer distance, as defined previously for bulk, is for AA stacking which equals 0.49 Å, the same as that in bulk. For AB stacking the interlayer distance is 1~2 Å larger than that for AA stacking. As depicted in Fig. 1.3, AA stacking is 96~137 meV per formula more favorable than all other possible stacking types and hence it corresponds to the lowest energy configuration.

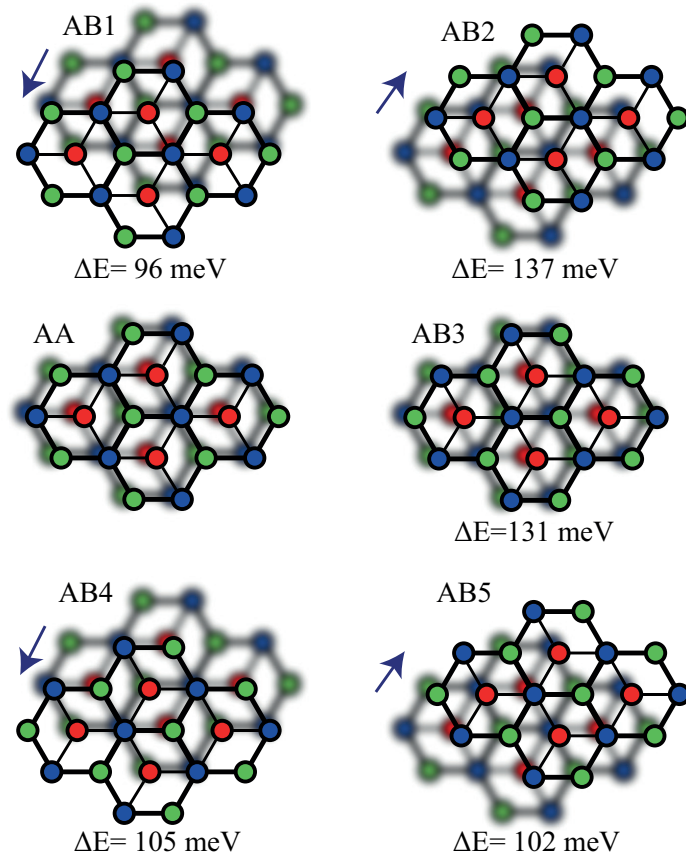


Fig. 1.3 Different stacked bilayers (bottom layer is blurred) and their energy difference with respect to the AA stacking of  $\text{Ca}(\text{OH})_2$ , i.e.  $\Delta E = E_{\text{ABX}} - E_{\text{AA}}$ , ( $X=1,2,\dots,5$ ). Energies are given per formula of  $\text{Ca}(\text{OH})_2$ . Blue, green and red circles are for Ca atom, upper hydroxyl group and lower hydroxyl group, respectively. For clarity, the bottom layer is shifted slightly.

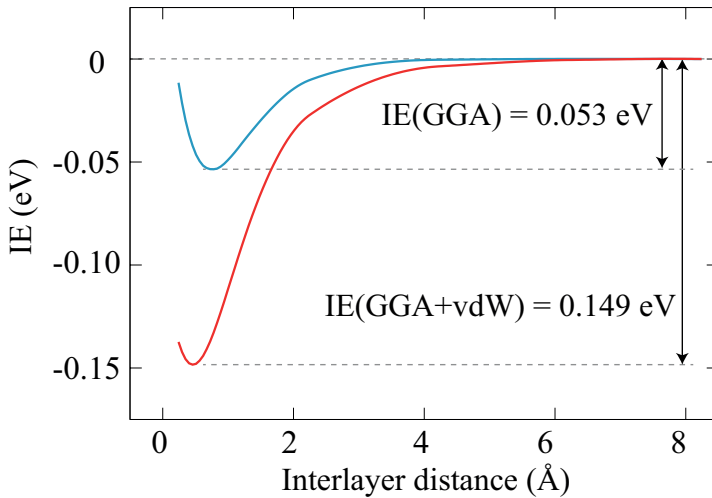


Fig. 1.4 Interlayer interaction energy per formula of AA-stacked bilayer  $\text{Ca}(\text{OH})_2$ . Blue and red curves are for GGA calculations without and with vdW correction, respectively.

To investigate the nature of the interlayer interaction, we have calculated the interlayer interaction energy (IE) for the AA stacked bilayer structure of  $\text{Ca}(\text{OH})_2$ . The IE is the energy difference between the total energy at a specific interlayer distance and that of a well separated bilayer. The plot of IE versus interlayer distance is shown in Fig. 1.4, where the energy of the well separated bilayer is defined as 0 eV. Two sets of calculations were performed, one set only considers GGA exchange correlation; while another set considers both the GGA and vdW interaction. At the optimized interlayer distance for the bilayer structure, almost 2/3 of the attractive interaction comes from the van der Waals interaction, and this is consist with D'Arco et al. [13] . They stated that interlayer interaction of Brucite, one of the isomorphous of Portlandite, is mainly a dispersion-type interaction. The nature of interlayer interaction in  $\text{Ca}(\text{OH})_2$  is mainly vdW type weak interaction. Our GGA+vdW calculations revealed that the interlayer interaction between two layers of  $\text{Ca}(\text{OH})_2$  (149 meV per formula) is much stronger than that of bilayers of  $\text{MoS}_2$  (76 meV per formula).

### Electronic properties

Our Bader charge transfer analysis showed that the final (initial) electron charge on Ca, O and H atoms after (before) the formation of the crystal are 6.4e (8.0e),

7.4e (6.0e) and 0.4e (1.0e), respectively. Therefore, in the bulk structure of  $\text{Ca(OH)}_2$ , Ca-O bonds, which are mostly in ionic character, are formed through 0.8e charge transfer from each Ca to O atom. Charge transfer is kept unchanged when it comes to the monolayer structure, except for the rest charge on H atom is 0.6e in monolayer.

Our calculations on the electronic structure reveal that bulk  $\text{Ca(OH)}_2$  is an insulator with a 4.37 eV direct band gap. As shown in Fig. 1.5 (a), the valence band maximum (VBM) and the conduction band minimum (CBM) are located at the  $\Gamma$  point. The partial density of states (DOS) shown in Fig. 1.1 (b) indicates that the major contribution to the states at the valence and conduction band edge originates from the O atoms, while deeper in the conduction band, states are mainly composed of the orbitals of Ca. The orbital character of a state at a particular band can also be deduced from a band and  $k$ -point decomposed charge density. As seen from Fig. 1.5 (c), edges in the top of VBM have  $\text{O-}p_x$  and  $\text{O-}p_y$  orbital character, and the hybridization of these states are also shown in the same figure. While the CBM has some  $p_z$  orbital character from the O atoms, but as the energy of the state increases, the  $d$  orbitals from Ca atom start to contribute, see ⑧ in the same figure.

Electronic properties of  $\text{Ca(OH)}_2$  are quite different from similar two-dimensional graphene-like structures. Unlike TMDs (such as  $\text{MoS}_2$  and  $\text{WSe}_2$ ) that exhibit indirect-to-direct band gap crossover when going from bulk to a single layer structure,  $\text{Ca(OH)}_2$  is a direct band gap semiconductor which is independent of the number of layers. Although the energy band gap at the  $\Gamma$  point decreases from 4.03 to 3.67 eV for a monolayer structure, electronic dispersion of the valence band edge remains almost unchanged, see Fig. 1.5 (d). As shown in Fig. 1.5 (e) the conduction states mainly originate from Ca atoms, while the valence states are mainly composed of the orbitals of O atoms.

Our magnetic state analysis shows that unless a defect is formed in/on the structure, there is no spin polarization in the ground state of both bulk and monolayer  $\text{Ca(OH)}_2$ . Therefore,  $\text{Ca(OH)}_2$  is a non-magnetic insulator regardless of its dimension for the structure.

Moreover, it was seen that the spin-orbit interaction has no considerable effect on the bond lengths and the overall electronic dispersion (except for a 26 meV splitting in the VBM at the  $\Gamma$  point, see Fig. 1.5 (f)). Due to the presence of

inversion symmetry of  $\text{Ca(OH)}_2$ , the degeneracy of spin-up and spin-down states still remains, this is also confirmed by the results of our calculation.

Band and  $k$ -point decomposed charge density in Fig. 1.5 are kept with the same isosurface level for comparison. However, as we further reduced the isosurface level at ④ in (d) and (g) of Fig. 1.5, which is the lowest conduction band of the monolayer at the  $\Gamma$  point:  $E_{c1}^{\Gamma}$ , charge density forms a planar state parallel to the layer on both sides, see Fig. 1.6 (a), this is also the case for the second lowest non-spin-resolved conduction band at the same  $k$ -point:  $E_{c2}^{\Gamma}$ , see Fig. 1.6 (b). These two states are important due to their unique character and having energy right below ionization energy. Such exceptional states having free-electron-like dispersion were reported before[29, 30] for doped graphite. To study the trend in these states, the same states were plotted for bilayer  $\text{Ca(OH)}_2$ , see (c) and (d) in Fig. 1.6.  $E_{c1}^{\Gamma}$  and  $E_{c2}^{\Gamma}$  have lower energies than ionization energy. Therefore, electrons are still close and bond to both sides of monolayers as seen from charge density. In the case of bilayer, interestingly, these states appear only on one side of bilayer.

### Mechanical properties

We present the quantities that describe the mechanical properties of  $\text{Ca(OH)}_2$  in table 1.2. At first, the in-plane Young's modulus of the bulk structure is calculated. Bulk  $\text{Ca(OH)}_2$  has a in-plane Young's modulus (55.0 N/m) and in-plane shear modulus (21.23 N/m). Both these quantities indicating flexible nature to in-plane tensile and shear deformation of bulk  $\text{Ca(OH)}_2$ . In addition, bulk  $\text{Ca(OH)}_2$  has an in-plane Poisson's ratio of 0.30. Additionally, the value of the in-plane stiffness for bulk  $\text{Ca(OH)}_2$  is calculated to be 60.1 J/m<sup>2</sup>.

If we go from bulk to bilayer  $\text{Ca(OH)}_2$ , we see a reduction in either the in-plane Young's modulus or the in-plane shear modulus, which are 50.7 N/m and 19.16 N/m, respectively. The in-plane Poisson's ratio on the other hand is slightly increased to 0.32 and become more spongy-like as opposite to more cork-like character[31]. In addition, the in-plane stiffness value of bilayer  $\text{Ca(OH)}_2$  is calculated to be 55.6 J/m<sup>2</sup>.

We found that monolayer  $\text{Ca(OH)}_2$  has a quite low in-plane Young's modulus (50.7 N/m) when compared to BN (278.2 N/m). The in-plane Poisson ratio (0.33) and the in-plane shear modulus (19.08 N/m) of the monolayer are similar

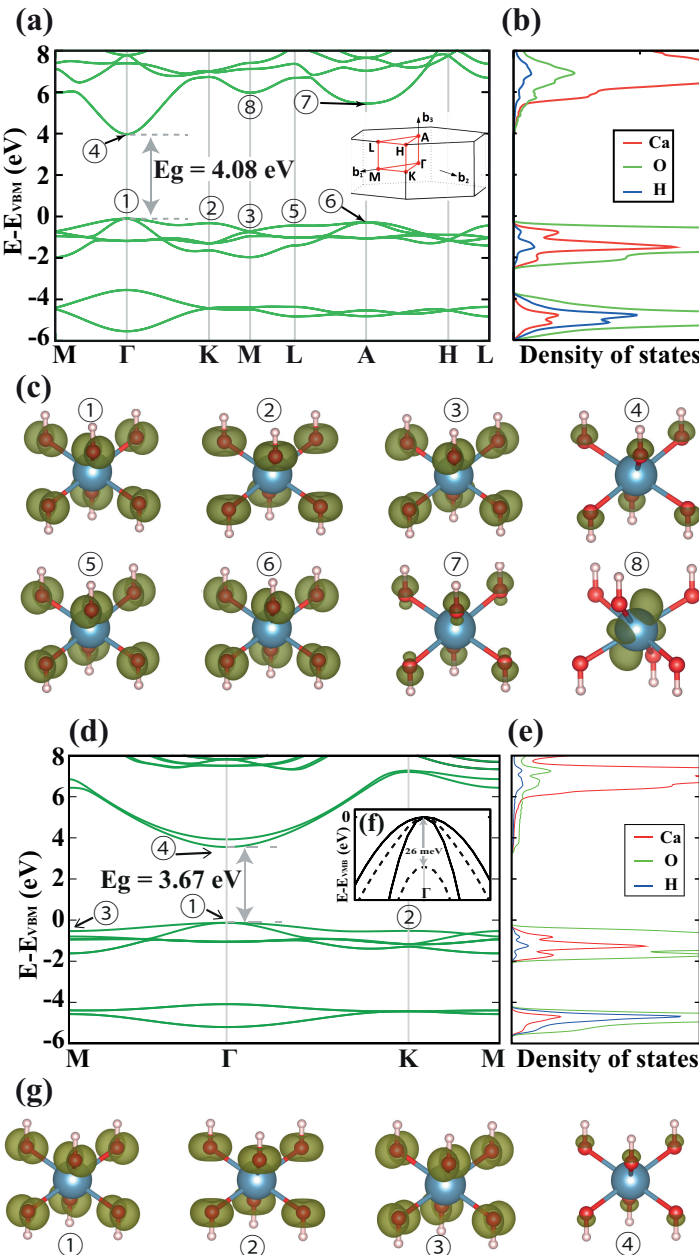


Fig. 1.5 (a) and (d) are the Band structures, (b) and (e) are the partial DOS and (c) and (g) are the band and  $k$ -point decomposed charge densities of the bulk (c) and monolayer (g)  $\text{Ca}(\text{OH})_2$ , respectively. The charge density are the band edges indicated in (a) and (d), isovalues are kept constant. (f) Band structure around  $\Gamma$  point is shown with (dashed line) and without (solid line) spin orbit coupling.

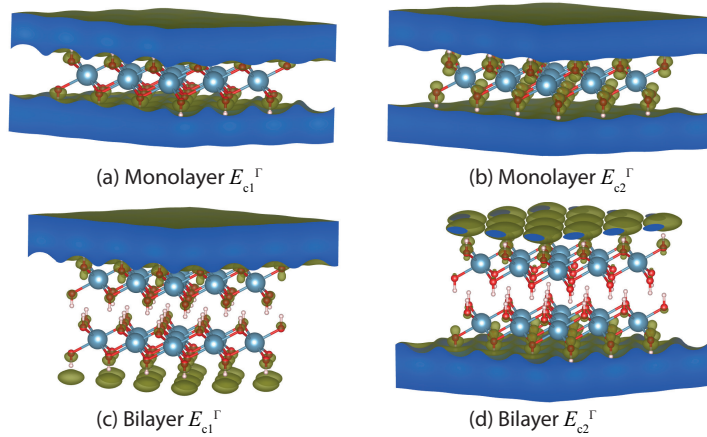


Fig. 1.6 Two lowest conduction band charge density of monolayer and bilayer  $\text{Ca}(\text{OH})_2$  at the  $\Gamma$  point.

with those for bilayer, and for BN, they are 0.22 and 113.5 N/m respectively. The calculated values of the in-plane stiffness of monolayer  $\text{Ca}(\text{OH})_2$  is 53.2 J/m<sup>2</sup>.

### Vibrational properties

Lastly, for the analysis of the vibrational spectrum and further examination of the dynamical stability of monolayer  $\text{Ca}(\text{OH})_2$ , we performed a calculation of the phonon spectrum using both the first-principles small displacement methodology (SDM)[18] and density functional perturbation methodology (DFPT)[32]. Here the non-quadratic dispersion of the flexural mode around the zone center is directly related to the insufficient FFT grid along the vacuum direction. It is seen from Fig. 1.7 that similar to the Raman shift measurements observed from the bulk crystal structure, monolayer material has also high-frequency OH stretching modes at 3700-3800 cm<sup>-1</sup>.

Further analysis of the analysis of phonon branches shows that the decomposition of the vibration representation of optical modes at the zone center is  $\Gamma = 4E_u + 2A_{2u} + 4E_g + 2A_{1g}$ . As shown in right panel of Fig. 1.7 there are four Raman-active phonon branches around 240, 350, 390 and 3700-3800 cm<sup>-1</sup>. It is also worth to note that differing from other TMD structures having 1T phase, presence of H atoms results in existence of two different  $E_g$  and  $A_{1g}$  modes.

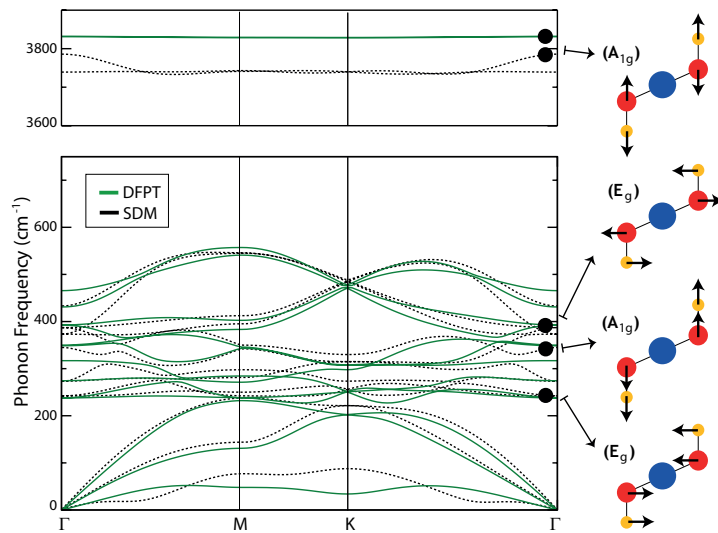


Fig. 1.7 Phonon dispersion of monolayer  $\text{Ca}(\text{OH})_2$ .

Here the phonon dispersion having real eigenfrequencies in the whole Brillouin Zone, which is another indication of the stability of monolayer  $\text{Ca}(\text{OH})_2$ .

### summary

By performing first principle calculations on bulk, bilayer and monolayer  $\text{Ca}(\text{OH})_2$  and experimental confirmation of the bulk crystal layered structure, we have predicted several important properties of this material and their stability. We found that: (i)  $\text{Ca}(\text{OH})_2$  crystals are environmentally stable and their stable structures can be synthesized by experimental methods; (ii) Experimentally, we also demonstrated that  $\text{Ca}(\text{OH})_2$  crystals can be grown in layered form and also be exfoliated on arbitrary substrates; (iii) The dimensionality of  $\text{Ca}(\text{OH})_2$  will not change the electronic, structural and magnetic properties qualitatively, nevertheless intrinsic mechanical stiffness of each layer will become slightly stiffer as the system go from monolayer to bilayer. (iv) Interlayer interaction is mainly van der Waals dispersion-type force, and the strength of the interaction is stronger than that of similar layered materials (e.g  $\text{MoS}_2$  and graphite). (v) The conduction states which have a free-electron-like character may be utilized for high-mobility electron transfer.

We believe that the stable structure and the unique electronic properties of ultra-thin Ca(OH)<sub>2</sub>, predicted for the first time here, will trigger interest in this new class of materials.

### 1.1.2 Few-layer of pentasilicene<sup>2</sup>

#### Introduction

Recently, a new 2D structure for carbon was proposed, called penta-graphene[33]. This crystal is composed entirely of pentagonal rings of C atoms with mixed sp<sup>2</sup>/sp<sup>3</sup> orbital hybridization. However, the silicon counterpart of this structure, penta-silicene, contains a dynamical instability in its monolayer form. A few attempts have been made to stabilize this new Si structure by hydrogenation[34] and chemical doping[35].

In the present work, we construct multilayer structures of penta-silicene. We use density functional theory to explore their stability and physical properties. Two types of stacking for the penta-silicene layers are found to give stable few-layer structures. These different stacking types lead to completely different electronic properties since one leads to metallic and the other to semiconducting behavior. Somewhat surprisingly, we found that bilayer penta-silicene has lower formation energy than the most stable hexagonal silicene bilayers. Furthermore, we found that the band gaps of these semiconducting penta-silicene bilayers can be tuned by mechanical strain. We first explore the stability of monolayer penta-silicene and demonstrate its dynamical instability. This forms the motivation to study few-layer systems. Then we investigate different stacking possibilities and the resulting stability. Further, we study their mechanical properties by calculating their elastic constants. We also compare bilayer penta-silicene to the most stable bilayer hexagonal silicene structures. Lastly, The electronic properties of multilayered penta-silicene are discussed.

#### Computational details

**Simulation program:** VASP and Phonopy

**Energy cut-off:** 500 eV

**Pseudopotentials:** PBE-GGA(PAW)

---

<sup>2</sup>This work is published in: P2.

**k points (Monkhorst-Pack):**  $17 \times 17 \times 1$  and  $23 \times 23 \times 1$  for insulating and metallic systems, respectively

**Vacuum:** 20 Å

**Energy and force convergence criterion:**  $10^{-8}$  eV and  $10^{-7}$  eV/Å, respectively

**phonon calculation:** finite displacement method

**Supercell for phonon calculation:**  $4 \times 4 \times 1$  and  $3 \times 3 \times 2$  for few-layer and bulk systems, respectively

**Ab initio molecular dynamics:** Parrinello-Rahman (NpT) dynamics [36, 37] and a Langevin thermostat [38]

**Ab initio molecular dynamics (Energy cut-off):** 300 eV

**Ab initio molecular dynamics (time step):** 2 fs

**Ab initio molecular dynamics (temperature):** 100 K

**Ab initio molecular dynamics (simulation time):** 6 ps

### Monolayer pentasilicene

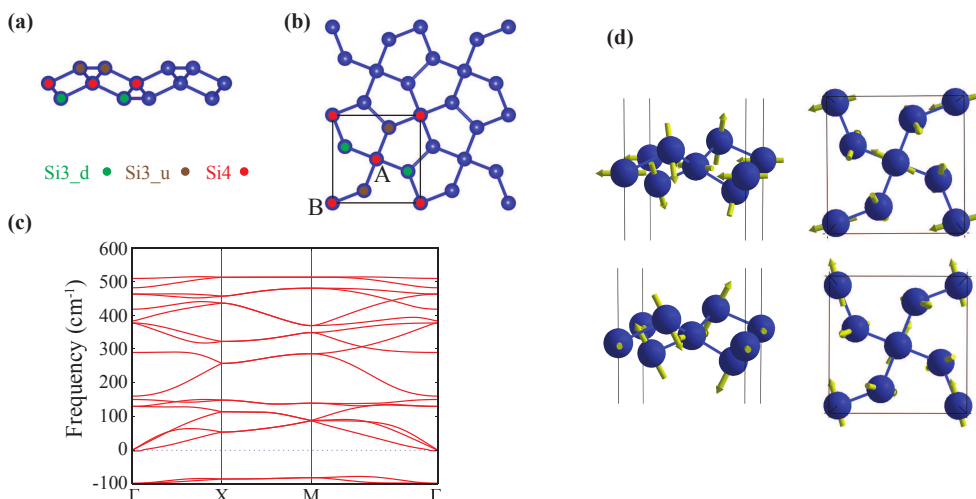


Fig. 1.8 (a) Side view and (b) top view of the atomic structure, (c) phonon spectrum and (d) two vibration modes with imaginary frequency of monolayer penta-silicene. Visualization of vibration modes is done with the V\_Sim package [39].

The layer group symmetry of monolayer penta-silicene (p-Si) is  $p\bar{4}2_1m$  (58). As shown in Fig. 1.8(a) and Fig. 1.8(b), the primitive cell contains six silicon atoms, of which two have fourfold coordination (Si4) and four have threefold coordination (Si3). Two of the Si3 atoms reside above the Si4 atoms, denoted as Si3\_u,

while the other two are below the Si4 atoms, denoted as Si3\_d. The Si4 atoms are bonded to four Si3 atoms while the Si3 atoms are connected to two Si4 atoms and one neighboring Si3 atom. Note that the two Si4 atoms have equivalent environments which are rotated by approximately 41° with respect to each other. Therefore, in analogy to graphene, we can relate these two equivalent Si4 atoms to sublattices which in the following will be referred to as the A and B sublattice.

The dynamical stability of this structure can be studied through its phonon spectrum. As noted before[34, 35] the phonon spectrum of monolayer p-Si contains imaginary frequencies as shown in Fig. 1.8(c), which is a clear signature of its instability. The corresponding atomic vibrations of the two imaginary frequencies at the  $\Gamma$  point are shown in Fig. 1.8(d). These modes correspond mainly to out-of-plane vibrations of the Si3 atoms with respect to the Si4 atoms. As a consequence, the structure is found to fall apart, indicating that there is no stable form of monolayer p-Si. However, the addition of extra layers could reduce these out of plane vibrations and stabilize the structure. This is the motivation to study few-layer p-Si.

### Multilayers of pentasilicene structures

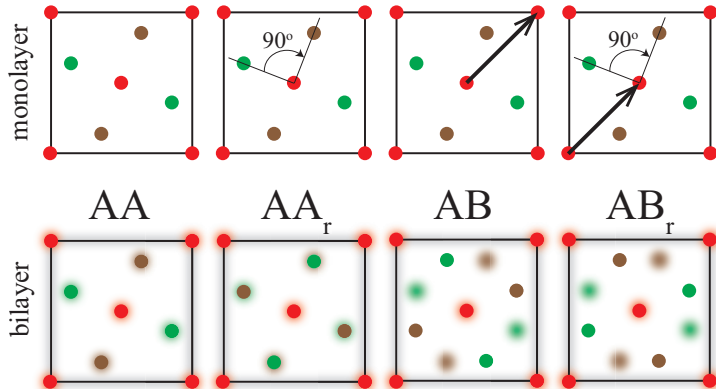


Fig. 1.9 Schematic illustration of the four stacking types for bilayer p-Si. The colors of the symbols correspond to those of the monolayer in Fig. 1.8(a) and Fig. 1.8(b). The bottom layer in the bilayer is blurred for clarity. The arrow represents translation and the angle represents the rotation of the top layer with respect to the bottom layer.

Table 1.3 The cohesive energy ( $E_{coh}$ ), the interlayer binding distance ( $d_{inter}$ ), the interlayer binding energy ( $E_{inter}$ ), number of interlayer bonds ( $N_b$ ) and energy per bond ( $E_{bond}$ ) of the four possible stacking types of bilayer p-Si. The interlayer binding energy per unit cell is defined as  $E_{inter} = E_{bi} - 2E_{mono}$ .

structure	$E_{coh}$ (eV/atom)	$d_{inter}$ (Å)	$E_{inter}$ (eV)	$N_b$	$E_{bond}$ (eV)
AA	-4.129	0.795	-3.502	4	-0.875
AA <sub>r</sub>	-4.113	2.379	-3.318	2	-1.659
AB	-3.968	2.174	-1.574	2	-0.787
AB <sub>r</sub>	-4.147	1.893	-3.725	2	-1.862
AB <sub>r</sub> <sup>d</sup>	-4.185	1.896	-4.174	2	-2.087

When considering two layers, different stacking configurations are possible. Here we focus on the so-called AA and AB stacking modes of the aforementioned sublattices (see Fig. 1.9). The stacking in which both layers have the same in-plane orientation and the Si atoms are put right on top of each other is called AA stacking. AB stacking arises by shifting the A sublattice of one layer to the B sublattice of the other. This nomenclature was also used by Wang et al. [40] for bilayer penta-graphene. Although penta-silicene has a terragonal lattice symmetry, the highest proper rotational symmetry order is two. Therefore, there are also two different possible orientations of the upper layer with respect to the lower one: One in which the two layers have the same orientation and another in which one layer is rotated over 90° with respect to the other one. We denote this last orientation with a subscript *r* to show that it results from a 90° rotation, e.g. AA<sub>r</sub>. Therefore, there are four possible stacking types for bilayer p-Si. Note that AB<sub>r</sub> stacking corresponds to the recently proposed bulk T12 phase for group IVA elements[41]. However, as discussed in more detail below, perfect AB<sub>r</sub> stacking is not stable in the case of multilayer penta-silicene. A considerable distortion of the outer layers is required to stabilize AB<sub>r</sub> stacking. The distorted structure, which will be referred to as AB<sub>r</sub><sup>d</sup> in the following, is obtained by breaking the symmetry between the two Si3 atoms at each surface side in AB<sub>r</sub> multilayers. In this way, one of the two Si3 atoms acquires sp<sup>2</sup> hybridization and loses an electron to the other Si3 atom that has sp<sup>3</sup> hybridization.

In table 1.3, we compare the energies of the different stacking modes. In all cases the Si4 atoms are not involved in interlayer bonding since their possible

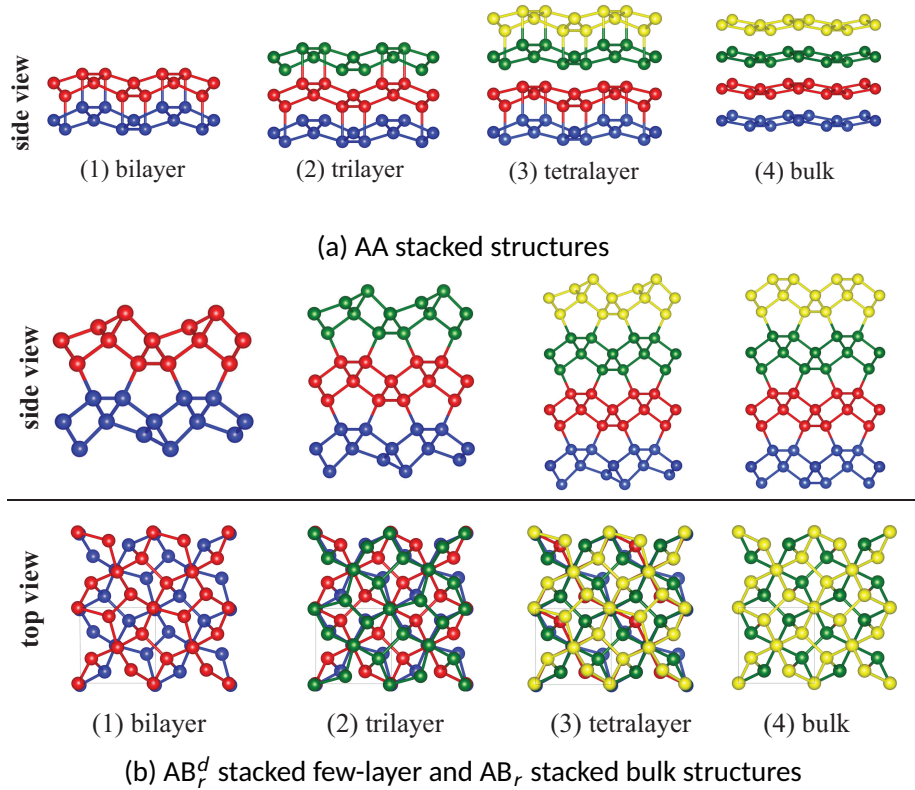


Fig. 1.10 Atomic structure of the  $2 \times 2$  supercell of few-layer p-Si. The number of atomic layers in the bulk structure is fixed to four for comparison (i.e.  $2 \times 2 \times 4$  and  $2 \times 2 \times 2$  supercells for AA and  $\text{AB}_r$  stacked bulk p-Si). (Visualisation using VESTA [42]).

number of bonds is already saturated. Except for the AA stacking where all Si<sub>3</sub> atoms are bound to Si<sub>3</sub> atoms from the other layer, only half of the Si<sub>3</sub> atoms are bonded to the other layer in the other cases. In table 1.3, the size of the interlayer binding energy and the strength per bond are given. The size of the bond energies indicate strong chemical bonding. The  $\text{AB}_r^d$  stacking mode clearly forms the most stable structure. For the rest of the paper, we will only focus on the most stable AA and AB-type stacking, i.e. AA and  $\text{AB}_r^d$ .

Table 1.4 The layer (space) group for few-layer (bulk) systems. The lattice constant ( $a$ ), the interlayer distance ( $d_{\text{inter}}$ ), the nearest-neighbor bond length range ( $d_{\text{min/max}}$ ), the cohesive energy ( $E_{\text{coh}}$ ), and the band gap (PBE) of few-layer and bulk p-Si.

stacking	structure	layer/space group	$a$ (Å)	$d_{\text{inter}}$ (Å)	$d_{\text{min}}$ (Å)	$d_{\text{max}}$ (Å)	$E_{\text{coh}}$ (eV/atom)	band gap (eV)
AA	- monolayer	$p\bar{4}2_1m$ (58)	5.587	-	2.233	2.363	-3.837	0.046 ( $M \rightarrow \Sigma$ )
	bilayer	$p\bar{4}2_1m$ (58)	5.907	0.795	2.363	2.468	-4.129	metal
	trilayer	$p\bar{4}2_1m$ (58)	5.887	1.085	2.330	2.606	-4.108	metal
	tetralayer		5.980	0.996/1.794 <sup>a</sup>	2.368	2.478	-4.150	metal
$AB_r^d$	bulk	$P\bar{4}2_1m$ (113)	6.234	1.769	2.398	2.463	-4.204	metal
	bilayer	$pb2b$ (30) $pm2a$ (31)	5.222	1.896	2.303	2.403	-4.185	0.119 ( $M \rightarrow \Sigma$ )
	trilayer	$p1$ (1)	5.222	1.989	2.298	2.413	-4.291	0.247 ( $M \rightarrow \Sigma$ )
	tetralayer	$pb2b$ (30) $pm2a$ (31)	5.221	1.997	2.298	2.413	-4.345	0.232 ( $M \rightarrow \Sigma$ )
$AB_r$	bulk	$P4_2/nmc$ (138)	5.220	1.999	2.358	2.413	-4.508	1.329 ( $M \rightarrow \Delta$ )

<sup>a</sup> The first and the second number indicate the interlayer distance between two monolayers and two bilayers, respectively.

We also investigated the stability of trilayer, tetralayer and bulk p-Si structures by adding extra layers to the stable bilayers mentioned above, their structures are shown in Fig. 1.10a and Fig. 1.10b. We list their structural and energetic properties in table 1.4. Extra layers increase the cohesive energy per atom due to a smaller ratio of surface atoms. For AA stacking, adding a 4th layer to a trilayer system results in a double bilayer system with lesser bonding between them. Going to AA bulk, the interlayer interaction appears to be further reduced and the buckled layers become more flat. Adding extra layers to an  $\text{AB}_r^d$  bilayer results in similar structures in which the Si<sub>3</sub> atoms of the surface layers become distorted. For bulk, the undistorted AB<sub>r</sub> structure is found in which 4-fold symmetry is restored.

## Stabilities

In this section we investigate the stability of the different multilayer structures discussed above. Phonon calculations for the AA and AB<sub>r</sub> stacking modes reveal that only the AA bilayer is dynamically stable at low temperature. The extra bonds of the Si<sub>3</sub> atoms in AA-stacked structures effectively reduce out-of-plane vibrations and stabilize the structure. Although the AA-stacked bulk structure has weaker interlayer bonding, its phonon spectrum contains no imaginary frequencies, indicating its dynamical stability. The AB<sub>r</sub>-stacked layers, on the other hand, exhibit similar out-of-plane vibrations of the outermost Si atoms as a monolayer. For  $\text{AB}_r^d$ -stacking the distortion of the outermost layer removes the instabilities from the phonon spectrum, so that these structures are also dynamically stable.

It is also interesting to see whether these structures remain stable at finite temperature. To this end, we performed *ab initio* molecular dynamics calculations at a temperature of 100 K. The evolution of the cohesive energy as a function of simulation time is shown in Fig. 1.12. For comparison, the results for the dynamically unstable monolayer are also shown. The monolayer laterally shrinks and becomes a disordered multilayered system. The AA and  $\text{AB}_r^d$  bilayer systems, on the other hand, remain stable and retain their crystalline structure.

As a final stability check, we investigate the mechanical stability of bilayer p-Si which is determined by the elastic constants of the structures. If the elastic constants satisfy the necessary and sufficient Born criteria generalized by

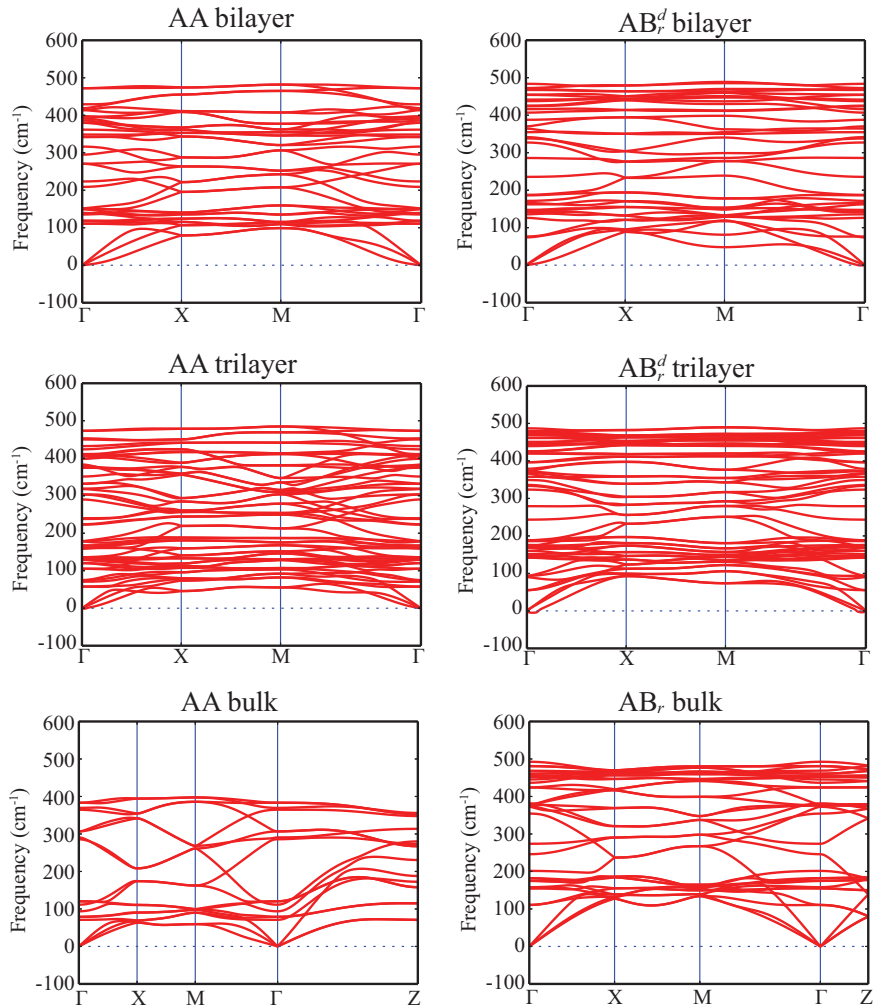


Fig. 1.11 Phonon spectra of different-stacked few-layer p-Si.

Mouhat and Coudert [43], the structures are mechanically stable. AA bilayer p-Si belong to the layer group symmetry of  $p\bar{4}2_1m$ , which belongs to the tetragonal symmetry groups, and the independent elastic constants in 2D are:  $C_{11}=101.43 \text{ N/m}$ ,  $C_{12}=36.36 \text{ N/m}$  and  $C_{66}=39.53 \text{ N/m}$ . In the case of  $\text{AB}_r^d$  bilayer p-Si, the crystal possesses pb2b or pm2a layer group symmetry which belongs to the orthorhombic crystal systems, and the independent elastic constants are:  $C_{11}=C_{22}=63.83 \text{ N/m}$ ,  $C_{12}=26.92 \text{ N/m}$  and  $C_{66}=50.43 \text{ N/m}$ . For mechanical stability, the following criteria must be fulfilled for 2D tetragonal systems:

$$C_{11} > |C_{12}|, C_{66} > 0, \quad (1.2)$$

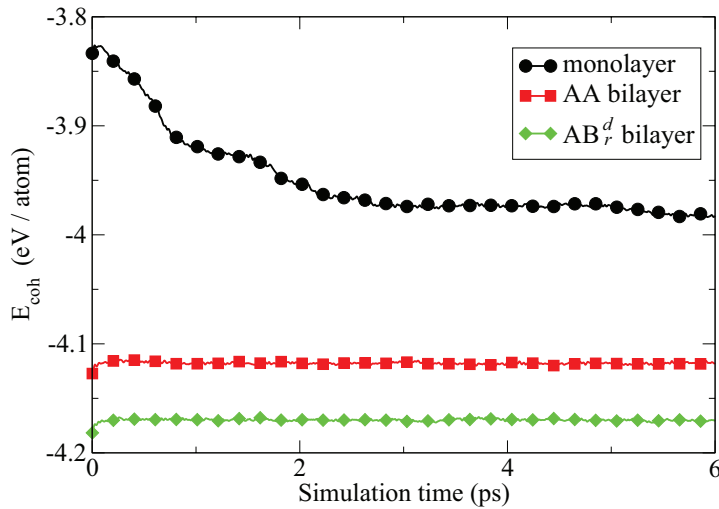


Fig. 1.12 The cohesive energy of monolayer and AA and  $\text{AB}_r^d$  stacked bilayer p-Si as a function of time at a temperature of 100 K under NpT-ensemble.

while 2D orthorhombic systems should satisfy:

$$C_{11} > 0, C_{11}C_{22} > C_{12}^2, C_{66} > 0. \quad (1.3)$$

As one can see, these criteria are satisfied by AA and  $\text{AB}_r^d$  bilayer p-Si which ensures their mechanical stability. Additionally, in table 1.5, we list the (2D) Young's modulus, shear modulus and Poisson's ratio of bilayer p-Si systems. An interesting aspect of the possion's ratio of  $\text{AB}_r^d$  is that it is quite high and close to the theoretical limit of 0.5. This means that this 2D material, prefers to change its shape rather than its surface area under strain, similar to the (3D) cases of rubber and water.

Table 1.5 Mechanical properties of  $\text{AB}_r^d$  bilayer p-Si

Stacking	$E[\text{N/m}]$	$G[\text{N/m}]$	$\nu$
AA	88.40	39.53	0.36
$\text{AB}_r^d$	52.47	50.41	0.42

### Relative phase stability

In this section we compare the cohesive energy of bilayer p-Si to the more familiar bilayer hexagonal silicene structures (h-Si). We examined 3 different stacking

types for h-Si bilayers, denoted as h-Si1, h-Si2, and h-Si3. To the best of our knowledge, these are the most stable hexagonal bilayer structures of silicene predicted so far. The h-Si2 structure corresponds to the re-DL-Si structure suggested by Morishita et al. [44] and the h-Si3 is the hex-OR- $2\times 2$  structure that was recently proposed by Sakai and Oshiyama [45]. These structures are constructed from the structure information provided by the authors in the supplementary material of the corresponding papers and re-optimized with our computational procedure. The h-Si1 is a new stable bilayer h-Si structure that we discovered (see ESI† for details). It is composed of two planar, non-buckled, compressed hexagonal silicene planes that are shifted along the crystal plane. This structure is interesting because although its cohesive energy is close to the former two cases, it has a non-buckled nature. To the best of our knowledge, it is the most stable non-buckled bilayer silicene discovered so far.

The cohesive energies of all the stable bilayer Si systems are given in table 1.6. It is seen that the  $\text{AB}_r^d$  bilayer p-Si system has the lowest energy, about 10 meV/atom less than the most stable hexagonal silicene bilayer h-Si3. This means that the  $\text{AB}_r^d$  p-Si structure is the most stable bilayer silicon structure predicted so far, which is a very surprising result. The AA-stacked p-Si has slightly higher energy than h-Si2 and h-Si3.

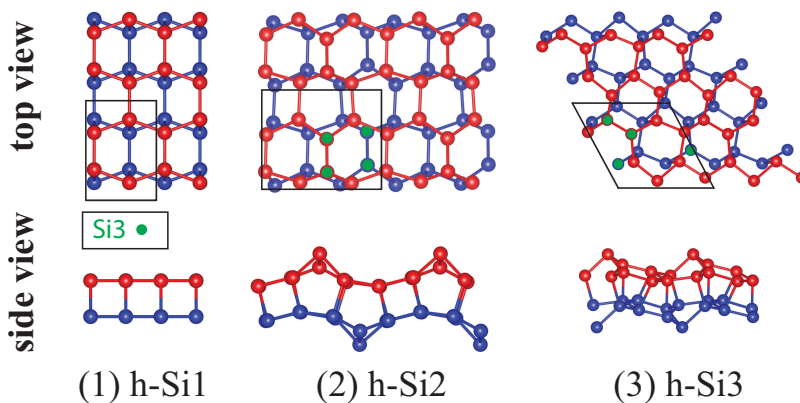


Fig. 1.13 Top and side views of the atomic structures of the  $2 \times 2$  supercell of the three examined hexagonal silicene bilayers.

Table 1.6 The interlayer distance  $d_{\text{inter}}$ , the nearest-neighbor bond length range ( $d_{\text{min/max}}$ ) and the cohesive energy per atom  $E_{\text{coh}}$  of the most stable hexagonal bilayer silicene and bilayer p-Si.

structure	$d_{\text{inter}}$ (Å)	$d_{\text{min}}$ (Å)	$d_{\text{max}}$ (Å)	$E_{\text{coh}}$ (eV/atom)
AA bilayer p-Si	0.795	2.363	2.468	-4.129
AB <sup>d</sup> bilayer p-Si	1.896	2.303	2.403	-4.185
h-Si1	2.175	2.358	2.418	-4.115
h-Si2	1.579	2.298	2.453	-4.165
h-Si3	1.378	2.288	2.473	-4.175

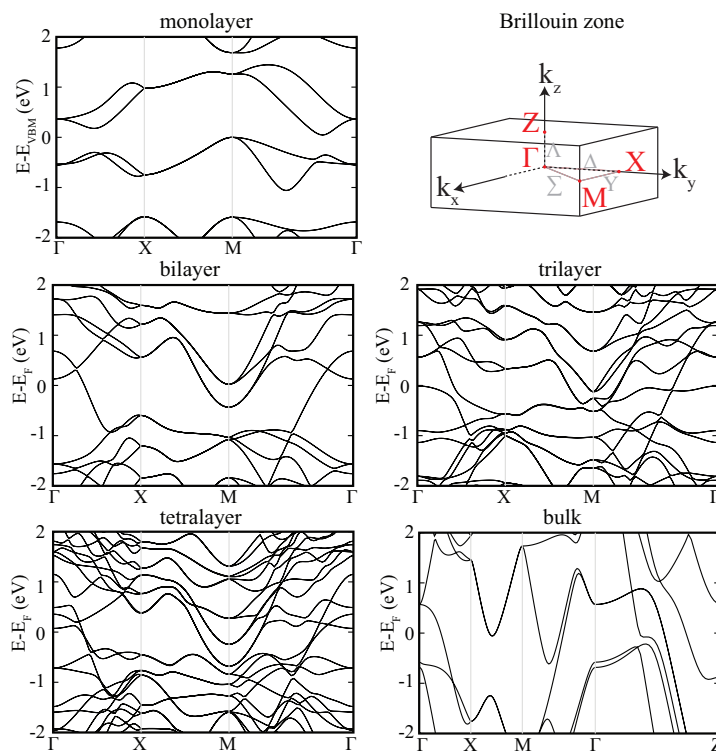


Fig. 1.14 Electronic band structure of AA stacked few-layer and bulk p-Si, and a schematic of the first Brillouin zone.

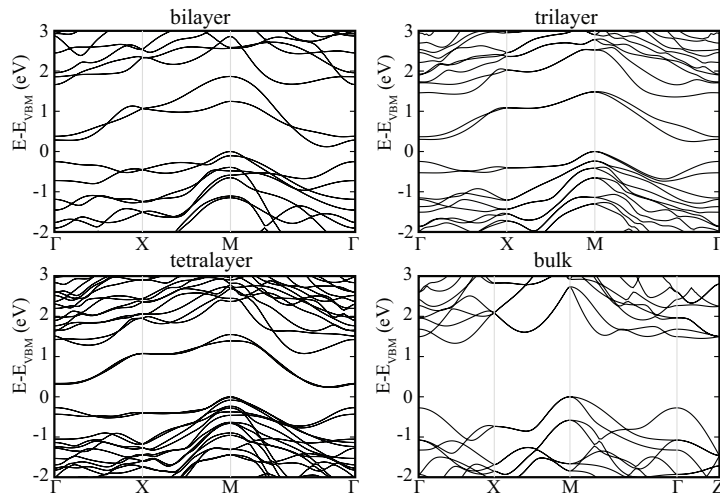


Fig. 1.15 Electronic band structures of  $\text{AB}_r^d$  stacked few-layer and  $\text{AB}_r$  stacked bulk p-Si. The results for the monolayer are shown for comparison.

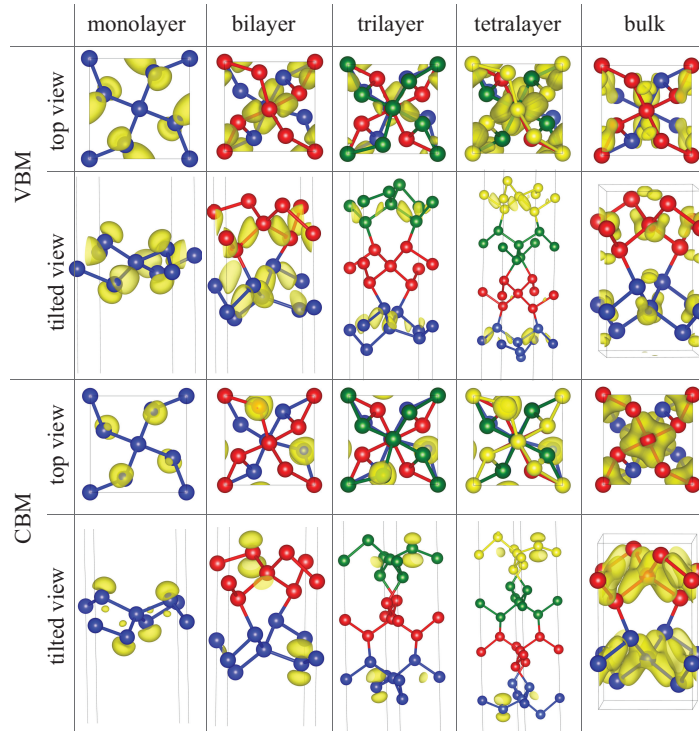


Fig. 1.16 The charge distribution of CBM and VBM in  $\text{AB}_r^d$  stacked few-layer and  $\text{AB}_r$  stacked bulk p-Si. The results for the monolayer are shown for comparison.

## Electronic properties

In the last part of this work, we investigate the electronic properties of few-layer and bulk p-Si. These electronic properties are mainly determined by the electronic spectrum. In Fig. 1.14 and Fig. 1.15, the electronic band structure of respectively AA and  $\text{AB}_r^d$  p-Si multilayers and their bulk counterpart is shown. The band structure of the unstable monolayer is also calculated for comparison. Monolayer p-Si is an indirect semiconductor with a band gap of 0.046 eV (PBE). The band-edge states are mainly composed of  $p_z$  orbitals of Si3 atoms. In contrast to this, all AA-stacked multilayers are metallic. In the case of the  $\text{AB}_r^d$  structure, the semiconducting properties of monolayer p-Si are preserved, but the band gap changes somewhat with the number of layers. This can be understood from the position of the electron and hole states which correspond to the conduction band minimum (CBM) and the valence band maximum (VBM), respectively. As seen in Fig. 1.15, the VBM and CBM states are always localized on the outermost layers. In other words, the electronic properties are mainly determined by the surface region which is nearly independent of the slab thickness. For  $\text{AB}_r$ -stacked bulk p-Si, there is no surface and the VBM and CBM correspond to bulk states. This explains the much larger band gap (1.33 eV) in the bulk case.

## Summary

In this work, we proposed several stable structures for few-layer pentasilicene. The stability of these structures was confirmed via their phonon spectrum, finite-temperature molecular dynamics, and their mechanical properties. The type of stacking mode, AA or AB, of few-layer pentasilicene has a crucial influence on the electronic properties: AA-stacked systems are metallic, while  $\text{AB}_r^d$  stacked ones are semiconducting. Surprisingly, the  $\text{AB}_r^d$  stacked bilayer pentasilicene has lower energy than the most stable bilayer hexagonal silicene structures, which makes it the most stable predicted form of bilayer silicon.

## 1.2 Mechanical strain

### 1.2.1 Carrier mobility enhancement in $\text{TiS}_3$ monolayer with strain<sup>3</sup>

#### Introduction

Recently, a number of two-dimensional (2D) crystal materials beyond graphene [46–48] have been synthesized or have been theoretically predicted to be stable. For example, transition metal dichalcogenides (TMDs) [49–54], phosphorene family [55–60], transition metal carbides/carbonitrides (Mxenes)[61], and penta-graphene [33] have attracted a growing research interest. Many of these materials have distinct properties with respect to their bulk counterpart, ranging from the nature of the band gap[62] to the size of the thermal conductivity [63]. For future electronic device applications, it is the high mobility and band gap of these materials, which has drawn significant attention of the researchers. Although graphene is a fascinating material due to e.g. its ultra high mobility, it has however one significant disadvantage, i.e. it lacks a band gap, and thus is unsuitable for digital electronic applications. This drawback has triggered extensive efforts to search for new materials having a finite band gap and high mobility. Recently synthesized phosphorene and monolayer  $\text{TiS}_3$ [64, 65] are examples of such promising materials for high-performance applications. On the other hand, the modification of physical and chemical properties through various methods, e.g. chemical functionalization, heterostructure and mechanical strain, could pave a path for the exploration of the hidden features which do not manifest themselves at the pristine structure.

Enhancement of the mobility under strain has been reported and measured before for silicon layers on  $\text{Si}_x\text{Ge}_{1-x}$  substrates [66, 67], according to which a mobility enhancement up to about 76 % at room temperature was achieved. Recently, first-principles calculations have been frequently used to determine the intrinsic mobility of 2D materials.[68–70]. There are also several works that investigated the mobility of monolayer materials under strain[71–73]. Inspired by significant improvements of the transport properties of 2D materials by the help of appropriate strain type and size, we investigate the strain dependence of carrier mobility of  $\text{TiS}_3$  monolayer under mechanical strain at 300 K. We find

---

<sup>3</sup>This work is published in: P3.

that more than an order of magnitude enhancement of the electron mobility can be achieved by the tensile strain. Furthermore the hole mobility also has moderate enhancement.

### Computational details

We perform first-principles calculations in the framework of density functional theory (DFT) as implemented in the Vienna *ab-initio* simulation package (VASP) [74–77]. The projector augmented wave (PAW) method is used to take into account the electron-ion interaction[78, 79]. Since the calculated mobility are strongly sensitive to the accuracy of the calculation, we use a set of input parameters that promise to deliver highly accurate results. Such crucial parameters are 700 eV energy cut-off for the plane wave basis set,  $10^{-8}$  eV for self-consistent total energy convergence,  $10^{-7}$  eV/Å for the ionic step force convergence,  $25 \times 25 \times 1$   $k$ -point mesh for the Brillouin zone sampling, and a large vacuum space of 20 Å between periodic images along the  $c$  direction that is perpendicular to the  $\text{TiS}_3$  layer. Exchange-correlation interactions are treated with the generalized gradient approximation (GGA) within the Perdew-Burke-Ernzerhof (PBE) formulation [80, 81]. Band gap is underestimated due to well-known semilocal functional band gap problem. However, for the position shifts of the valence and conduction band edges with an applied tensile strain, the semilocal functional can provide consistent results and trends when compared to hybrid functionals and has been successfully used in previous studies for the determination of the mobility in 2D material [70, 71, 82]. Phonon calculations are performed in a supercell of  $2 \times 3 \times 1$  using the finite displacement method as implemented in VASP together with the PHONOPY program [83].

To determine the mobility of electron and hole, we use the deformation potential theory together with the effective mass approximation [84], which has been previously applied to several 2D systems[85–88]. The mobility,  $\mu$ , of a 2D system is given by:

$$\mu = \frac{2e\hbar^3 C}{3k_B T |m^*|^2 E_d^2}. \quad (1.4)$$

where  $e$  is the electron charge and  $\hbar$  is the reduced planck constant.  $C$  is the elastic modulus along the transport direction. It is defined as  $C = (\partial^2 E_{total} / \partial \varepsilon^2) / S_0$ , where  $E_{total}$  is the calculated total energy of  $\text{TiS}_3$ ,  $\varepsilon$  is the strain applied along the

transport direction and  $S_0$  is the equilibrium 2D area of the unit cell.  $k_B$  is the Boltzmann constant. T is the temperature, which is equal to 300 K throughout the paper unless stated otherwise.  $m^*$  is the effective mass of the carrier along the transport direction calculated from  $1/m_{e(h)}^* = \partial^2 E_{c(v)}(k)/\partial k^2 \hbar^2$ , where  $E_{c(v)}(k)$  is the energy dispersion near the CBM (VBM).  $E_d$  is the deformation potential constant (DPC) along the transport direction. It is defined as  $E_d^{e(h)} = \Delta E_{CBM(VBM)}/(\delta l/l)$ , where  $\Delta E_{CBM(VBM)}$  is the energy shift of the band edges with respect to the vacuum level under a small dilation  $\delta l$  of the lattice constant  $l$ . We fix  $\delta l/l$  to 0.005 that is inspired from previous calculations [87]. In this theory, the dominant scattering process is the longitudinal acoustic phonon scattering (AS). However, for a polar material, scattering on optical phonon modes and other scattering sources should be taken into account at high temperatures[68]. Nevertheless, in this work, we will focus solely to the effect of AS to mobility and its dependence on the strain for the following reasons: 1) The dominant role of AS is not suppressed in polar materials, so it is still an important part that determines the mobility, 2) To separately study different mobility-controlled mechanism, specially their strain dependence, and 3) Computationally less expensive.

### Unstrained system

As is shown in Fig. 1.18, monolayer TiS<sub>3</sub> is a direct band gap semiconductor having a band gap of 0.29 eV (1.06 eV [87]) calculated with PBE (HSE06) functional at the  $\Gamma$ -point. The conduction band minimum (CBM) has the largest contribution from  $d_{x^2-y^2}$  and  $d_{z^2}$  orbitals of the Ti atoms, while the valence band maximum (VBM) is mostly dominated by the  $p_x$  orbital of the S atoms and the  $d_{xz}$  orbitals of the Ti atoms. The  $x$  and  $y$  directions coincide with the  $a$  and  $b$  directions, respectively. The  $z$  direction is taken perpendicular to the  $xy$  plane. Later, we will discuss in detail how these states change their energies when they are exposed to the mechanical strain.

To gain deep insight about the binding nature in the TiS<sub>3</sub> monolayer, we calculate the Bader charges[20–22, 89]. According to the Bader analysis, each Ti atom donates 1.61 e<sup>−</sup> to eight S atoms surrounding it. Each of the surface S atoms, labelled as S1 in Fig. 1.18, binds only with two Ti atoms and gain 0.34 e<sup>−</sup> net charge. Two of these S1 atoms form a covalent bond between them. While each of the S atom between two Ti layers, S2 in Fig. 1.18, binds with four neighboring

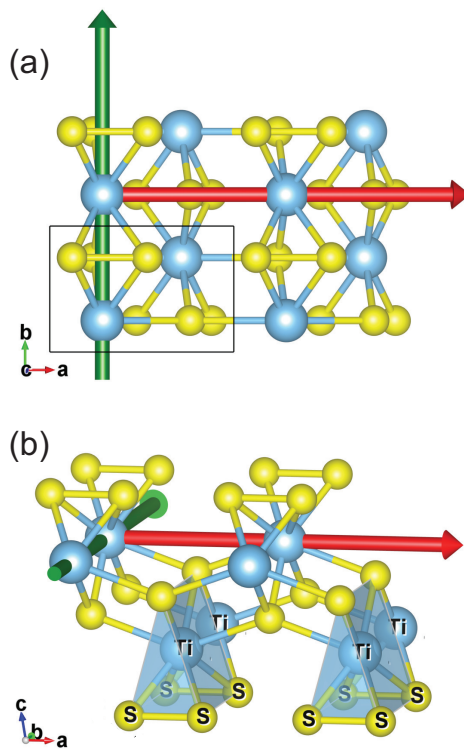


Fig. 1.17 (a) Top and (b) tilted views of a  $2 \times 2$  supercell of monolayer  $\text{TiS}_3$ . Two crystallographic directions (where the strain is applied or the mobility is calculated) are shown with red and green arrows.

Ti atoms, and have  $0.81 \text{ e}^-$  net charge accumulated on it. The electronegativity differences between S (2.58) and Ti (1.54) is calculated as 1.04, which belongs to the polar covalent bond class [90]. This value is large as compared to that of  $\text{MoS}_2$  where Molybdenum (2.16) and S (2.58), which is 0.41 and is considered as covalent bond type.

Before applying strain to our system, we summarize the mobility and related parameters for the unstrained  $\text{TiS}_3$  in Table ??, which are in agreement with previous calculations [87]. Similar data for phosphorene are presented for comparison. The results for phosphorene are recalculated with the same computational parameters as  $\text{TiS}_3$ . The mobility of the electron in  $\text{TiS}_3$  monolayer has an impressive level, which is an order of magnitude larger than that in phosphorene. However, resulting from very small DPC, hole mobility in phosphorene is an order of magnitude larger than that in  $\text{TiS}_3$ . Moreover, the anisotropy of the ef-

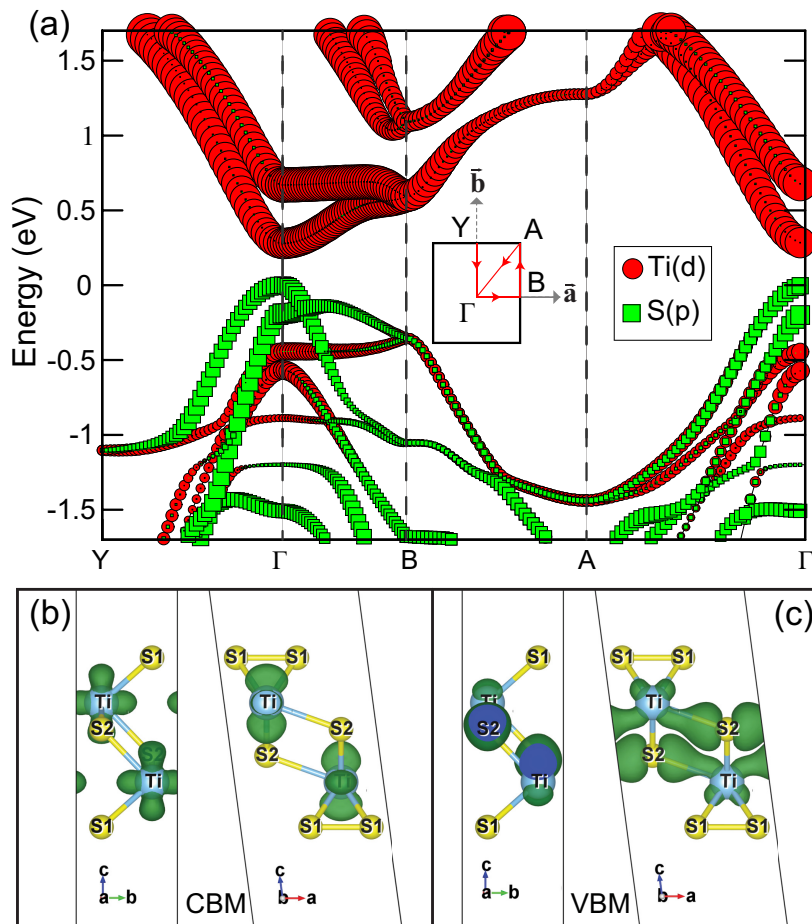


Fig. 1.18 (a) The site and orbital-projected band structure (calculated using PBE functional) of the unstrained  $\text{TiS}_3$  monolayer. Decomposed charge density of CMB (b) and VBM (c) at the  $\Gamma$  point are presented.

fective mass along different crystallographic directions is much more significant for phosphorene as compared to that in  $\text{TiS}_3$ . Phosphorene overall is softer than  $\text{TiS}_3$  as far as the elastic modulus is concerned.

### Dynamical stability under mechanical strain

Applying mechanical strain may have important effects on the stability of a structure. Therefore, it is crucial to know if strain applied to the system does not induce any structural instability. To this purpose, we calculate the elastic modulus and phonon spectrum for the  $\text{TiS}_3$  monolayer under various strain values

in order to confirm its dynamical stability. Figure 1.19 shows the elastic modulus along the *a* and *b* directions as a function of applied strain. These values correspond to the elastic constants, i.e.  $C_{11}$  and  $C_{22}$ . Here,  $C_{11}$  ( $C_{22}$ ) reflects the mechanical response of the TiS<sub>3</sub> monolayer to a strain applied along the *a* (*b*) direction. The calculated value of  $C_{11}$  ( $C_{22}$ ) for the unstrained TiS<sub>3</sub> is 133.76 (82.68) N/m, in good agreement with previous calculations [87, 91]. Note that the calculated elastic constants are all positive and they fulfill the mechanical stability criteria, i.e.  $C_{11}$  and  $C_{22} > 0$ . These results clearly imply that monolayer TiS<sub>3</sub> is less stiff than graphene and single layer h-BN, however, it is mechanically superior as compared to MoS<sub>2</sub> and phosphorene[92]. Furthermore,  $C_{22}$  is always larger than  $C_{11}$ , meaning that the *a* direction is stiffer than the *b* direction.

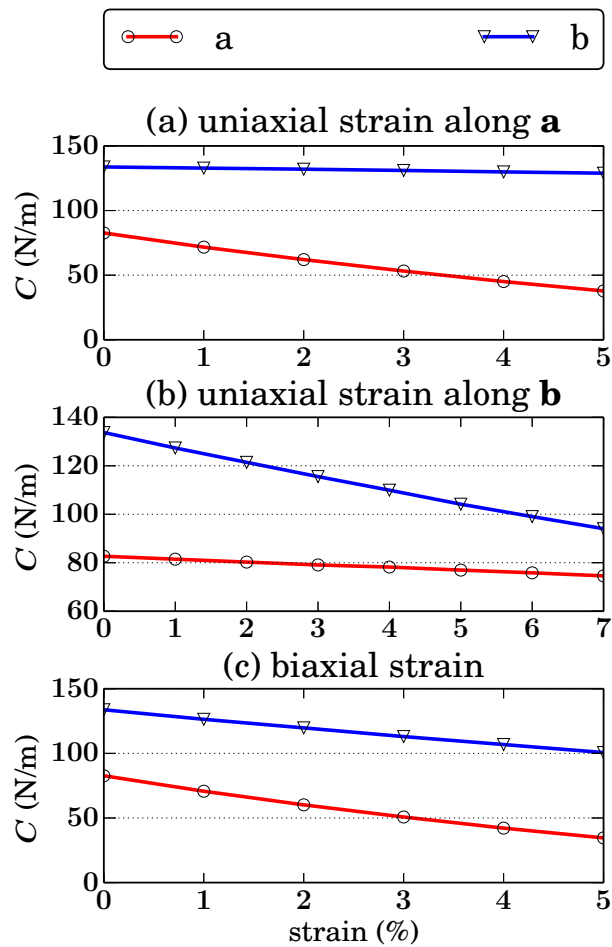


Fig. 1.19 Calculated elastic modulus along the *a* and *b* directions under mechanical strain.

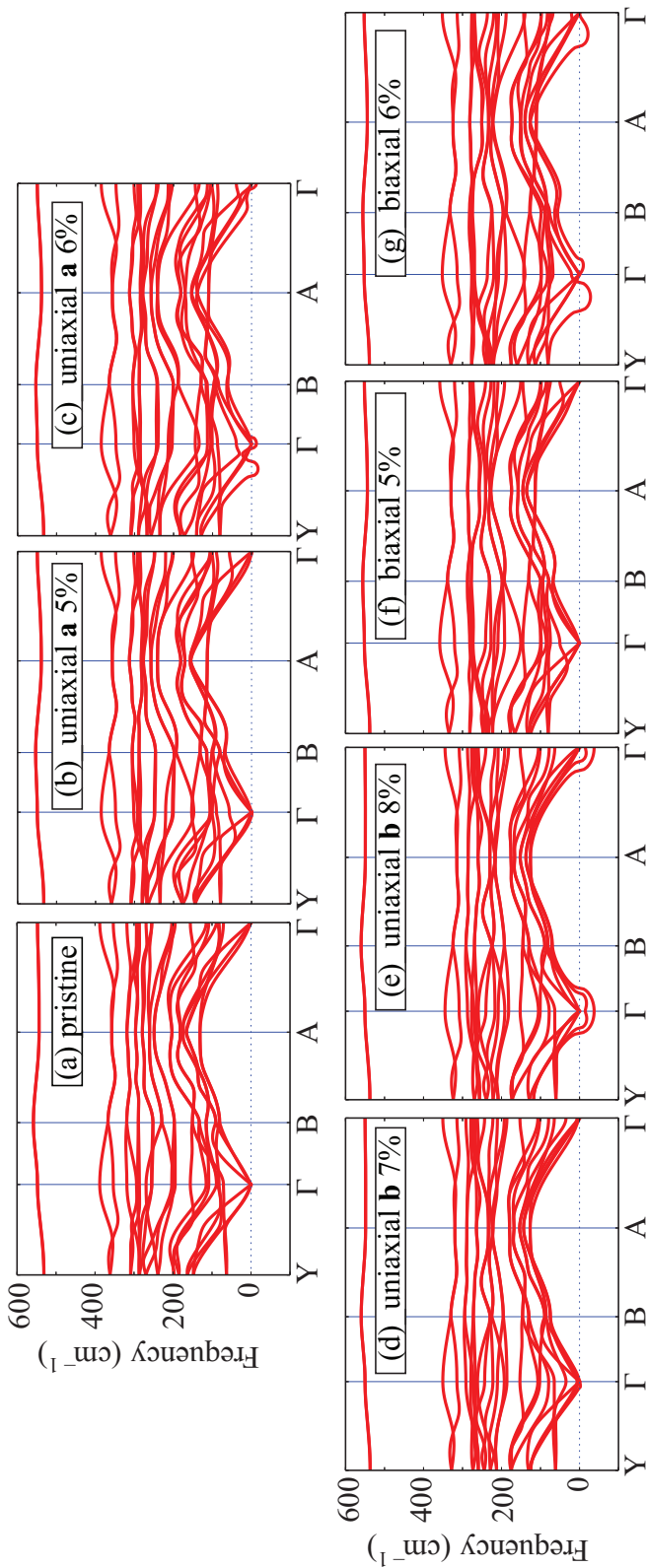


Fig. 1.20 Calculated phonon spectrum of (a) pristine monolayer TiS<sub>3</sub> and that under strain (b-g).

In order to gain further insight into the stability of  $\text{TiS}_3$  monolayer, we calculate the phonon dispersion under different types of strain. As shown in Fig. 1.20, uniaxial strain applied along the  $a$  and  $b$  direction induce dynamical instability in the system at strain values of 6% and 8%, respectively. Note that the highest optical mode reaches up to  $550 \text{ cm}^{-1}$  and does not vary with strain. Consistency with our results of the elastic constants, the optical phonon modes are more sensitive to strain applied along the  $b$  direction, see Fig. 1.20. Except for the topmost mode, phonon branches move downward with strain applied along the  $b$  direction. We observe an average downward shift of  $25 \text{ cm}^{-1}$  at 8%, which should be easily detected by Raman spectroscopy. The observed instability at large strain values is due to the presence of imaginary vibrational frequencies, suggesting a structural phase transition. The dynamical stable range of black phosphorus is 15% which is much larger than that of  $\text{TiS}_3$ [93]. Due to its puckered structure, the former is able to sustain large mechanical deformations. The biaxial case is the combination of two uniaxial strains applied along the  $a$  and  $b$  directions, and the stable range is determined by the lowest strain value, i.e. 6% applied along the  $a$  direction.

### Bond lengths and band gap under mechanical strain

The foremost consequence of the mechanical strain is the change of the structure parameters in the unit cell. Strain is applied by manually changing the lattice constant along the desired direction. After that, the cell parameters are kept fixed whereas the internal atomic positions are allowed to fully relax. Therefore, the latter can be considered as the response of the material to the external strain, which would carry important information about the consequential effects. The variation of the bond length provides information about how the local environment of atoms in the unit cell changes with strain. Considering this, we plot the bond lengths with respect to the different types of strain in Fig. 1.21.

In the following discussion, we correlate the variation of the CBM and VBM, as shown in Fig. 1.22, with the change of bond length by investigating their bonding character. Let us first focus on strain applied along the  $a$  direction. The most significant change occurs for the Ti-S bond between two neighboring prisms. As the strain increases, the local environment inside the prism hardly changes, whereas the bond lengths of Ti-S bonds between prisms. On the other hand, it

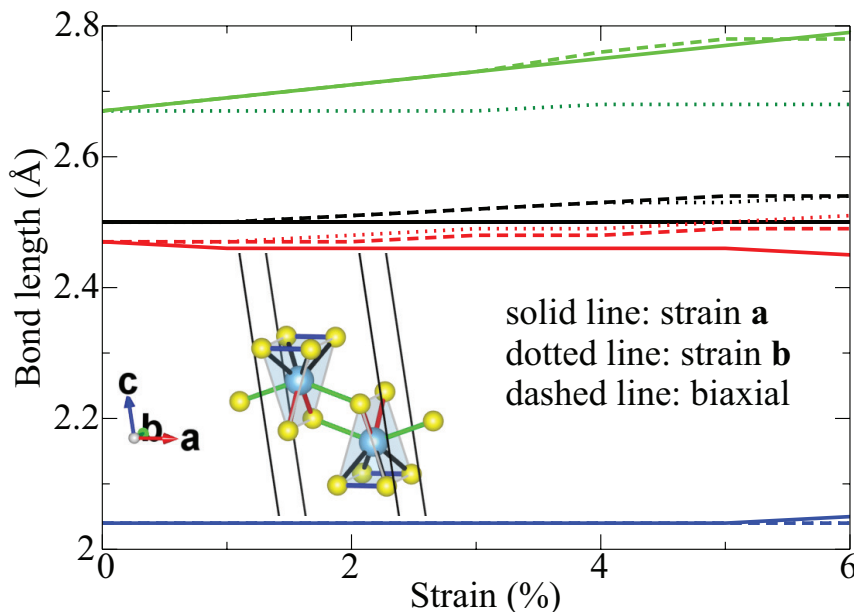


Fig. 1.21 Variation of bond lengths with strain. Color of the curves matches with the color of the bonds in the structure depicted in the inset.

can be seen from the decomposed charge density of the VBM at the  $\Gamma$  point for the unstrained TiS<sub>3</sub> (see Fig. 1.18(c)) that the Ti-S distance between two prisms is controlled by the Ti-S bonding state at the VBM. Therefore, we would expect that the energy of this state increases (i.e. its binding energy decreases) with tensile strain, which can be seen in Fig. 1.22. For strain applied along the *b* direction, one can note from Fig. 1.18(c) that the VBM charge distribution along the *b* direction has a node between two prisms. Given the fact that atoms sit close to each other, this is an anti-bonding state. Therefore, we would expect that its energy decreases (i.e. its binding energy increases by depopulating the anti-bonding state) when strain along the *b* direction increases. This is true when we see the trend of the VBM with the strain applied along the *b* direction in Fig. 1.22. The CBM mostly gives a nonbonding state regardless of the direction, see Fig. 1.18(b). This results in a much slower variation of the energy of the CBM under tensile strain, yet only an overall small change is observed.

Figure 1.22 also provides information about the variation of the band gap under strain, which agrees well with previous calculations [94, 95]. While the band gap decreases under strain applied along the *a* direction, it increases with

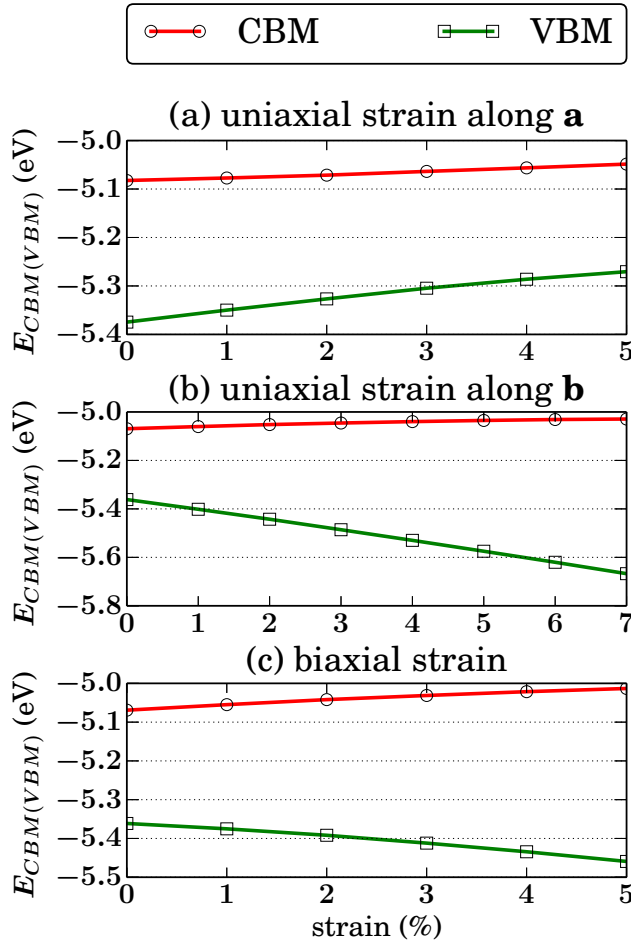


Fig. 1.22 Variation of the band edges with respect to vacuum with strain.

strain applied along the  $b$  direction. The band gap increase in the latter case was experimentally confirmed [94]. By the help of strain engineering, it is possible to tune the optical gap from far infrared to near infrared. The nature of the band gap remains direct within the considered tensile strain range where  $\text{TiS}_3$  is dynamically stable. We find that biaxial strain is a superposition of the above two situations as can be seen from Fig. 1.22.

### Effective mass, deformation potential constant and mobility under mechanical strain

Using the computational setup described above, we estimate the acoustic-phonon-limited mobility of monolayer TiS<sub>3</sub> under strain via Eq. (1.4). According to this equation, at a particular temperature (e.g. 300 K), three different physical parameters, namely elastic modulus  $C$ , carrier effective mass  $m^*$  and DPC or  $E_d$ , are subjected to a change under strain. Previously, we already discussed the variation of the elastic modulus with strain, which is shown in Fig. 1.19. Now we discuss how the effective mass and DPC change under strain. Figure 1.23 shows the effective mass of both hole and electron for different directions and strain values. All curves change monotonically. There is no abrupt change of the slope of the curves since there is no band crossing in the considered strain range, and one would expect a smooth variation for the band edges with strain. The electron mass along the  $a$  direction increases regardless of the direction of applied strain, and the magnitude of this change is the largest among both carrier effective masses along the other directions. Because of this, the degree of anisotropy in the effective mass increases as TiS<sub>3</sub> is subjected to strain. As for the hole effective mass, the difference along the  $a$  and  $b$  directions increases for strain applied along the  $a$  direction whereas this difference decreases for strain applied along the  $b$  direction. Such anisotropy can be utilized to modify the electronic and thermoelectric properties of TiS<sub>3</sub>.

Our calculations unveil that one of the most important factors that determines the mobility is the DPC. In order to evaluate DPC, we need to apply a small dilation along the direction where DPC is calculated. The ratio of the CBM (VBM) shift to the amount of this dilation gives DPC for electron (hole), see Fig. 1.24. Mathematically, as shown in Eq. (1.4), it is the square of a small number in the denominator. Thus the variation of DPC determines the whole ratio in Eq. (1.4) thereby the mobility, unless other quantities change dramatically, which is not the case as we have discussed. For example, in the work of Fei and Yang [71], they reported the direction of the highest mobility change by 90°, which was a result of the change in the smallest effective mass in a particular direction. In our case, we observe no band crossing and the variation of the effective mass with strain is rather small for the highest mobility directions, see Fig. 1.23.

Next, we explore the mobility variation under strain, see Fig. 1.25. For uniaxial strain along the *a* direction, the two most apparent changes are the moderate enhancement of the hole mobility along the *b* direction, from  $2.00 \times 10^3$  to  $7.08 \times 10^3 \text{ cm}^2\text{V}^{-1}\text{s}^{-1}$  and the drop of the electron mobility along the same direction, from  $1.82 \times 10^3$  to  $0.25 \times 10^3 \text{ cm}^2\text{V}^{-1}\text{s}^{-1}$ . Although the electron mobility along the *a* direction for stainless TiS<sub>3</sub> is close to the hole mobility along the same direction, an order of magnitude difference can be realized by the help of tensile strain. Therefore, uniaxial strain applied along the *a* direction would be helpful to select carrier type based on their different transport properties. For uniaxial strain along the *b* direction, we find a dramatic enhancement of the electron mobility along the *a* direction, from  $1.71 \times 10^4$  to  $5.53 \times 10^5 \text{ cm}^2\text{V}^{-1}\text{s}^{-1}$  at 300 K. This corresponds to a mobility enhancement from  $5.13 \times 10^4$  to  $1.66 \times 10^6 \text{ cm}^2\text{V}^{-1}\text{s}^{-1}$  at 100 K. The subsequent drop at 7 % can be ascribed to being close to the edge of the dynamical stable region. Furthermore, the electron mobility in the other direction (i.e. *b*) has a moderate enhancement at strain value of 6 % as well. The electron mobility along the *b* direction has a considerable increase when tensile strain is applied along the *b* direction. The hole mobility generally tends to decrease on both directions. As stated before, the biaxial case is an effective combination of two uniaxial strains applied along the *a* and *b* directions. The electron mobility along the *a* direction reaches up to  $3.68 \times 10^5 \text{ cm}^2\text{V}^{-1}\text{s}^{-1}$  at 5% biaxial strain.

Lastly, we discuss the effect of the optical phonon scattering on the mobility. Using a Drude-like expression,  $\mu$  can be expressed as  $\sim q\langle\tau\rangle/m^*$ , where  $\langle\tau\rangle$  is the average scattering time, and in the Matthiessen's Rule, it is given as sum of all scattering process, i.e.  $1/\tau = 1/\tau_{ph} + 1/\tau_{el} + 1/\tau_{imp} + \dots$ . Here,  $\tau_{ph}$ ,  $\tau_{el}$  and  $\tau_{imp}$  are the scattering times related to electron-phonon, electron-electron and electron-impurity scattering, respectively. In a rough estimate (i.e using Einstein's model),  $\tau_{ph}$  for the longitudinal optical phonon scattering is inversely proportional to the frequency of the optical modes. According to our calculations, the frequency of the phonon modes is subject to a redshift under strain. This means that the contribution of the optical phonon scattering reduces with increasing tensile strain. As a result, we can claim that our trends are persistent against the contribution of the different scattering processes.

## Summary

In this work, we have demonstrated that, by the help of tensile strain, it is possible to enhance the carrier mobility of the  $\text{TiS}_3$  monolayer more than an order of magnitude at 300 K and two orders of magnitude at 100 K. Phonon dispersion calculations revealed that  $\text{TiS}_3$  becomes dynamically unstable for an uniaxial tensile strain larger than 6% (8%) applied along the  $a$  ( $b$ ) direction. The degree of effective mass anisotropy can be controlled with uniaxial strain. The deterministic role of the deformation potential constant on the mobility in this material is confirmed. The variation of the CBM and VBM with strain was explained through the bonding character within the  $\text{TiS}_3$  monolayer. Here, we also showed that strain engineering appears as a quite exciting way to tune the electrical conductivity of  $\text{TiS}_3$ , which is potentially useful for device applications including flexible electronics.

## 1.3 Heterostructures

Another way to explore the property land of materials is to combine different composites to form heterostructure[96–98]. They can be composites made by materials with complementary characters and perform better than each of the material individually, or materials those give new phenomenon and promising properties only when act together. Given the obvious structure anisotropic in 2D materials, there are two types of heterostructures: vertical or lateral, see for example Fig. 1.26. The vertical heterostructures composed of stacks of different 2D materials. They are held together via what holds graphite layers together: van der Waals force. Thus, this type of construction is referred as van der Waals heterostructures. On the other hand, lateral heterostructure[99, 100] is made by joining the edges of different 2D materials and the connection is mostly made through strong bonding, e.g. covalent or ionic. For this case, all the new properties results from the interface. In this section, I will present one for each type of the heterostructure and explore one properties. Comparisons will be made to illustrate the advantage of choosing these materials over the homo-structure.

### 1.3.1 Electrical transport in 1T/2H/1T MoS<sub>2</sub> lateral heterostructure<sup>4</sup>

#### Introduction

Heterostructures are the essential components of a wide range of solid-state devices, such as transistors, solar cells, and sensors[102, 103]. They are fabricated by combining different type of materials, e.g. metal, semiconductor, and insulator. Therefore, the physical properties of the combined system are enhanced or become more controllable as compared to that of each material individually. These tailored properties are strongly related to the interface of two different materials where all interesting and new phenomenon occur. However, along with the emergence of nanostructured materials, dimensionality has become another major factor affecting the physical properties of materials and devices along with the interface. Thus, solid-state device fabrication with heterostructures based on low dimensional nanomaterials has attracted significant attention and a new research area in material design has been initiated where researchers are expecting unprecedented results, phenomenon and physics[104-106]. Indeed, several advantages of two dimensional (2D) phase engineering over the three dimensional counterpart has already been demonstrated.[107]

In low dimensional heterostructure device architectures, there are usually two types of interfaces connecting different materials: top contact (vertical) and edge contact (lateral)[108]. In top contacts, an overlapping portion of two materials are glued together mainly via interlayer van der Waals (vdWs) interaction, while in edge contacts one dimensional edges of two materials are contacted with covalent bonds without overlapping. The van der Waals interaction in top contact introduces a potential gap between the two layers which electrons have to tunnel through, and resulting in higher resistance due to the reduced carrier transmission probability. Naturally, this resistance is much lower in edge contacts owing to the formation of covalent bonds that provides a path for carriers to travel across the interfaces[109, 110]. Recently, Eda *et al.* has discovered the coexistence of multi-phase MoS<sub>2</sub> that is a promising material for heterostructure device fabrication due to their natural metal-semiconductor-metal structure with clear edge contacts[111]. Considering the distinct electronic nature

---

<sup>4</sup>This work is submitted as: P5.

of these phases, physical properties of these heterostructures[112, 113] can be tuned by phase engineering and novel solid-state device architectures can be realized for several different future applications.

The same research group has synthesized two dimensional semiconducting heterostructure devices[33, 114] by using metal contacts. As a result of their experimental analysis, they have particularly pointed out the vital importance of the geometry and electronic nature consistency between the metal contact and the heterostructure on the device performance[111, 115]. Considering this fact, Kappera *et al.*[112] have locally induced 1T metallic phase of MoS<sub>2</sub> in the 1H semiconducting phase of it, and they measured that the edge resistance was lower than that of metal contacts by more than a factor of two. Subsequently, 1T|1H lateral heterostructure has been drawn peculiar attention as a promising contact structure having a higher carrier injection rate. Different arrangements of the interfaces between 1T and 1H phases was investigated through theoretical calculations[116, 117] and the structure formed by the connection of armchair edges of 1T and 1H phases has been determined as an energetically more favorable configuration. However, in these calculations, the more stable metallic structure (1T<sub>d</sub>), which arises with small distortion of 1T phase, was considered.

The present paper aims to investigate the electronic transport properties of MoS<sub>2</sub> multi-phase lateral junctions when the more stable metallic phase of MoS<sub>2</sub> ( i.e. 1T<sub>d</sub>) acts as the contact, which is compared with the 1T phase. Further to this, the paper mainly focuses on the effect of doping on the electrical transport properties. In the results section, we first construct three junction models and calculate their transmission without external bias . Then we calculate the electronic properties for different level of doping.

### **Computational details**

The presented first-principles calculations are based on density function theory as implemented in the Vienna *ab initio* Simulation Package (VASP) [74-77]. A plane-wave basis set based on the projected augmented wave (PAW) method [78, 79] are used to describe the wave functions. The cutoff energy of the basis is set to 400 eV. Exchange-correlation interactions are treated with the generalized gradient approximation (GGA) within the Perdew-Burke-Ernzerhof (PBE) formulation [80, 81]. A 25×25×1 *k*-points mesh is used to sample the Brillouin-

zone for monolayer structures of 1H, 1T and  $1T_d$  MoS<sub>2</sub> and a  $9 \times 1 \times 1$   $k$ -points grid is used for the structures shown in Fig. 1.27. A vacuum space of 15 Å is incorporated to avoid interaction between the periodic images. The energy convergence criterion for the self-consistent calculations is set to  $10^{-5}$  eV, while the force convergence criterion for the ionic steps is set to  $10^{-2}$  eV/Å.

Electronic transport across the  $1T_d/1T\text{-MoS}_2 | 1H\text{-MoS}_2$  interfaces is calculated using the self-consistent non-equilibrium Green's functions (NEGF) technique as implemented in TranSIESTA[118] which is interfaced with the SIESTA code.[119] Double-zeta (plus polarization) numerical orbital basis sets are used for all atoms. We employed norm-conserving pseudo-potentials[120], the GGA/PBE functional, and an energy cutoff for the real-space mesh of 250 Ry. In order to get accurate transmission spectra, the 2D Brillouin zone normal to the transport direction is sampled by meshes composed of 100  $k$ -points in the periodic direction. While the SIESTA code uses a localized basis set and norm-conserving pseudopotentials, the calculated lattice parameters for different phases of MoS<sub>2</sub> agree well with those obtained from the VASP code.

## Results

The use of metallic TMDCs as metal electrodes are expected to offer a breakthrough in the semiconductor industry as they have negligible heat dissipation and therefore are energy efficient. Among metallic TMDCs, metallic phases of MoS<sub>2</sub> (1T- and  $1T_d$ -MoS<sub>2</sub>) have attracted a growing interest due to its smooth interface with the semiconductor phase of MoS<sub>2</sub> (1H-MoS<sub>2</sub>). However, 1H phase is thermodynamically more stable than both 1T and  $1T_d$  phases. Therefore, the stabilization of 1T and  $1T_d$  over 1H phase becomes an essential requirement for the successful experimental realization of device configurable structures such as  $1T/T_d\text{-MoS}_2 | 1H\text{-MoS}_2$ . On the other hand, 1T MoS<sub>2</sub> is the meta-stable and undergoes a Peierls transition to a low-energy state  $1T_d$  (or distorted 1T) and thus, metal contacts with the  $1T_d$  structure are more stable than the one with the 1T phase. However, the MoS<sub>2</sub>  $1T_d$  phase retransforms to the 1H phase at room temperature. As far as the relative stability is considered, choosing  $1T_d$  as metal contact further stabilized the junction. Therefore, understanding the effect of different physical mechanisms on the stability of multiple phases (H, T,  $T_d$ ) of this material is of vital importance to develop a proper control on phase

transitions. To this end we mainly focus on the effect of doping (either charge or atom) on the stability, electronic and transport properties of 1T/T<sub>d</sub>-MoS<sub>2</sub> | 1H-MoS<sub>2</sub> interfaces. For the 1T and 1H hexagonal unit cells, the optimized in-plane lattice constant is obtained as 3.18 Å. On the other hand, the optimized lattice constants are  $a=3.18\text{ \AA}$  and  $b=5.72\text{ \AA}$  for the tetragonal 1T<sub>d</sub> unit cell. These values are in good agreement with previous calculations[121]. It was previously discovered the coexistence of 1T<sub>d</sub> phase with other two phases indicating their experimental stabilities, yet it is also possible to relax the 1T<sub>d</sub> phase to 1T phase using external source, such as electron beam irradiation[111]. In experiment, 1T and 1T<sub>d</sub> are indistinguishable, because the S atoms are the same in two cases, only the Mo form cluster which STM image is limited to differentiate.

In this work, we systematically investigate the electronic and transport properties of three different device architectures, called as  $\alpha$ ,  $\beta$ , and  $\gamma$ , denoted in Fig. 1.27. In all device models, the semiconducting 1H-MoS<sub>2</sub> phase is sandwiched between two 1T<sub>d</sub> metal electrodes to create Schottky contacts at the interfaces. In the  $\alpha$  structure, the metallic part consists of both 1T and 1T<sub>d</sub>-MoS<sub>2</sub> phases. The size of metallic and semiconducting parts are larger than 20 Å along the transport direction. The interface between the 1T<sub>d</sub>-MoS<sub>2</sub> and 1H-MoS<sub>2</sub> phases have either an armchair termination as in the case of the  $\alpha$  and  $\beta$  structures, or a zigzag termination as in the case of the  $\gamma$  structure in order to investigate the influence of the contact type on the calculated properties. We predict that the  $\gamma$  structure significantly deviates from planar geometry after structural relaxation, see Fig. 1.27. To check whether such distortion is due to a calculation artifact, we started from a complete planar geometry and allowed both atomic coordinates and cell parameters relax to their equilibrium values (or lowest energy configuration). We observed that planar structure is not stable and structural relaxation brought back the original distorted structure. Indeed, such buckling or deviation from planar structure mainly restricts to the left interface, in line with a recent work that proposed a new crystal structure model for MoS<sub>2</sub>[121]. Observed buckling helps to reduce repulsive interaction between S atoms at the left interface, thereby enhancing the stability of this interface.

The transmission spectra for all three device models at zero bias are depicted in Fig. 1.28. In these plots, the Schottky barrier for holes (electrons) is defined as the difference between Fermi level and valence band maximum (conduction

band minimum) of the semiconductor 11HH phase of MoS<sub>2</sub>. The first clear observation is that there is a large barrier height at the pristine interfaces and there is no transmission within an energy range of 1.8 eV around the Fermi level, corresponding to the band gap of 1H-MoS<sub>2</sub>. The Schottky barrier heights for the  $\alpha$ ,  $\beta$  and  $\gamma$  structures are predicted as 0.72, 0.80, and 0.63 eV for holes and 1.16, 0.99 and 1.19 eV for electrons, respectively. The estimated size of the scattering region along the transport direction is larger than 23 Å, which is much smaller than the mean free path of electron in MoS<sub>2</sub>[122] and therefore, the transport properties of these systems can be estimated with ballistic transport calculations. The  $\beta$  structure has the largest transmission over the calculated energy range. The Mo atoms form a zigzag chain perpendicular to the interface (or along the transport direction) in the  $\beta$  and also  $\gamma$  structures which enhances the electrical transport in these systems. However, the non-symmetric Mo zigzag chain lying parallel to the transport direction leads to scattering of electrons at the interface and gives rise to low transmission as compared to the  $\alpha$  and  $\beta$  structures. Similar anisotropic electron transport has also been observed for ReS<sub>2</sub> where resistance is the lowest along the Re cluster direction[123]. Comparing the  $\alpha$  and  $\beta$  devices, the coexistence of 1T and 1T<sub>d</sub> regions in the former device contributes to lowering of the transmission due to additional scattering at the 1T/1T<sub>d</sub> interface as compared to the latter device where we only have 1T<sub>d</sub> phase in the electrode region.

We next turn to the calculations of the electronic properties as a function of doping. The central part of 1H-MoS<sub>2</sub> as the least affected from interface formation is considered to predict the band gap and the position of the band edges with respect to the Fermi level. The calculated band gap value, 1.75 eV, clearly indicates that the size of the 1H part is large enough to achieve the monolayer limit and eliminates the electrode-electrode interaction. In fact, the band gap of the pristine 1H-MoS<sub>2</sub> monolayer calculated with the same functional is around 1.7 eV. In line with the transport calculations, the Fermi level appears within the band gap of the central region of 1H-MoS<sub>2</sub>. The calculated Schottky barriers are 0.75 eV for holes and 0.99 eV for electrons in the  $\beta$  structure. In the following discussion, we mainly focus on the  $\beta$  structure due to its better transport properties as compared to the  $\alpha$  and  $\gamma$  devices. Other device models also exhibit similar properties. Our results contradicts experimental findings in the sense that, in

experiments, it was shown that 1T (or  $1T_d$ )|1H-MoS<sub>2</sub> interfaces exhibit a superior performance over the 3D metal-MoS<sub>2</sub> interfaces. However, we predict large Schottky barriers which give rise to a large contact resistance. In order to shed light on this contradiction, we calculate the electronic properties of the  $\beta$  structure as a function of electron doping. First of all, the electron doping stabilizes the  $1T_d$  phase over the 1H-MoS<sub>2</sub> and prevents the structural phase transition to the semiconducting 1H-MoS<sub>2</sub> phase[124]. Also, the electron doping decreases the Schottky barrier height for electrons at the interface, leading to the formation of *n*-type Schottky barrier. This is attributed to the increase of the density of electrons in the *d*-orbital of the metallic  $1T_d$  MoS<sub>2</sub> phase. Figure 1.30 shows the variation of the Schottky barrier as a function of the electron concentration. We find that the Schottky barrier already diminishes for electron concentration larger than 0.1 electron (per  $1T_d$  MoS<sub>2</sub> formula unit). The Fermi level rises about 1 eV when only 0.28 electron is placed on the  $1T_d$  part. The direct electron doping can be achieved by using electron beams in experiments or Li/Na adsorption on the metallic phase[124, 125]. Here, the considered alkali atoms donate their electron to the  $1T_d$  phase and enhance the stability and electronic properties of the metallic part[124]. In addition, absorption of hydrogen atom on the 1T part of MoS<sub>2</sub> has been also shown to reduce the barrier at the interface of 1T-MoS<sub>2</sub> |1H-MoS<sub>2</sub>[126, 127].

Another possible strategy to enhance stability of metallic phases and electrical conduction at the metal-semiconductor MoS<sub>2</sub> interface is to dope metallic phase with transition metal atoms. Most of the well known TMDCs are either in the 1H or 1T phase when in their ground state. However, the single layer ReS<sub>2</sub> has neither H nor T as ground state, it stabilizes in  $1T_d$  structure[53, 128]. Therefore, alloying MoS<sub>2</sub> with Re may stabilize the  $1T_d$  structure of MoS<sub>2</sub> and leads to *n*-type doping of the crystal as similarly proposed by Raffone *et al.* for Sn doped 1T phase[129]. Meanwhile, we have previously shown that doping of ReS<sub>2</sub> with Mo results in a *p*-type doping of ReS<sub>2</sub> monolayer[128]. Therefore, we investigate the effect of substitutional doping of Re at Mo sites of  $1T_d$ -MoS<sub>2</sub> on the transport properties. Here, we also consider the group V element Ta since the pristine TaS<sub>2</sub> monolayer crystallizes in the 1T phase and results in a *p*-type doped  $1T_d$  MoS<sub>2</sub> structure. Indeed, in a recent work, it was shown that distorted phase of MoS<sub>2</sub> becomes energetically stable over 1H phase when Re concentration ex-

ceeds 50%[130]. In this work, we did not consider such large dopant concentrations because of two reasons. First of all, lattice mismatch between 1H-MoS<sub>2</sub> and doped 1T-MoS<sub>2</sub> phases can be kept minimal for small dopant concentrations. At large concentrations, the relaxation of cell parameters leads to artificial enlargement of lattice parameters of 1H-MoS<sub>2</sub>. Secondly, Re doped 1T<sub>d</sub>-MoS<sub>2</sub> becomes a semiconductor. To show the effect of doping, we only considered concentrations smaller than 20%. In this work, we assumed that doping of 1T-MoS<sub>2</sub> with Re or Ta may avoid the structural transition to 1H phase due to, for instance, temperature effect. Figure 1.31 shows the PDOS for the central part of 1H-MoS<sub>2</sub> for Re and Ta doped  $\beta$  structure. In the case of Re doping, the Fermi level approaches the conduction band of 1H-MoS<sub>2</sub>, accompanying a significant decrease in *n*-type Schottky barrier height. On the other hand Ta doping reduces the *p*-type Schottky barrier height as expected. For a concentration of 14% (per electrode), the *n*-type Schottky barrier becomes 0.85 eV for Re and *p*-type Schottky barrier becomes 0.58 eV for Ta.

Since Re and Ta doping give rise to different electronic properties, we can design metal-semiconductor junctions with different type of Schottky barrier heights (i.e. *n*- and -*p* type) in the same device geometry. This allows us to design optical and photovoltaic applications. While a Re doped junction effectively blocks holes, Ta doped junction hampers the easy passage of electrons across the junction. In this device geometry, we can separate photo-generated charge carriers for instance. Figure 1.32 shows the device model and projected density of states as a function of position in 1H-MoS<sub>2</sub>. While the left electrode is doped with Re, the right electrode is alloyed with Ta. The central part of 1H-MoS<sub>2</sub> clearly has a PDOS similar to free standing 1H-MoS<sub>2</sub> monolayer with a band gap of 1.75 eV. However, we have different electronic properties in the right and left side of the central region. Due to Re (Ta) doping, the left (right) part has a *n* (*p*)-type Schottky barrier. The presence of 1T<sub>d</sub>-1H MoS<sub>2</sub> interfaces develops mid-gap states that mainly come from the atoms in the boundary region. The electronic properties gradually change from the metallic to the semiconductor when moving away from the interfaces. For the atoms far away from the interface region (i.e. central region of 1H-MoS<sub>2</sub>), we observe a clear band gap which is close to that of pristine 1H-MoS<sub>2</sub>. While the mid-gap states appear below the Fermi level at the left interface (Re-doped side), they are unoccupied and reside above the

Fermi level at the right interface (Ta-doped side). About 3.2 Å from the interface, the mid-gap states start to disappear.

Figure 1.33 shows the electrostatic potential along the heterojunction. We consider both pristine and doped  $\beta$ -devices. For undoped heterojunction, the average potential is symmetric at the left and right interfaces. However, doped heterojunction has a different electrostatic potential, especially, within 1H-MoS<sub>2</sub>. Due to its valence configuration, Re (Ta) acts as a donor (an acceptor). This is reflected in the average effective potential shown in Fig. 1.33(b). The average electrostatic potential (EP) does not have a sharp variation at the 1T<sub>d</sub>-1H interface, extending along the 2-3 atomic rows. This is due to fact that we form interfaces between two different crystal structures of MoS<sub>2</sub> (i.e 1T<sub>d</sub> and 1H). EP converges to the same value at the left and right electrodes. If one considers a photovoltaic device using the  $\beta$  structure co-doped with Re and Ta, an electron-hole pair is generated after absorbing a photon in the 1H part. Re-doped interface has a higher potential as compared to Ta-doped interface, producing a driving force for dissociation of the electron-hole pair. The electron flows along the potential decline (i.e. towards Ta-doped electrode) and the hole in the opposite direction (i.e. towards Re-doped electrode). In this way, a photocurrent can be generated by the photovoltaic effect. Thus, by proper control of doping and interface roughness, we can control the quantum efficiency of electron-hole dissociation[131].

## Conclusion

In this work, we explored the impact of doping on the electronic and charge transport properties across the 1T<sub>d</sub>-1H MoS<sub>2</sub> interfaces by considering various device models. Doping and alloying (with charge, atom or molecule) appear as an effective method to tailor and improve the physical-chemical properties and stabilities of not only 1T/1T<sub>d</sub> phases of MoS<sub>2</sub> but also other 2D materials. The interface structure between 1T<sub>d</sub> and 1H phases is one of the decisive factors in the determination of the electrical transport across the heterojunction. We found that the Schottky barrier height of electrons for pristine heterojunctions can even disappear as a result of electron doping. While charge doping only reduces the Schottky barrier for electrons, co-doping is able to tune the barriers for hole and electrons at the same time.

## 1.4 Defect induction

### 1.4.1 Faceted blue phosphorene nanotube formed by line defects<sup>5</sup>

---

<sup>5</sup>This work is published in: P4.

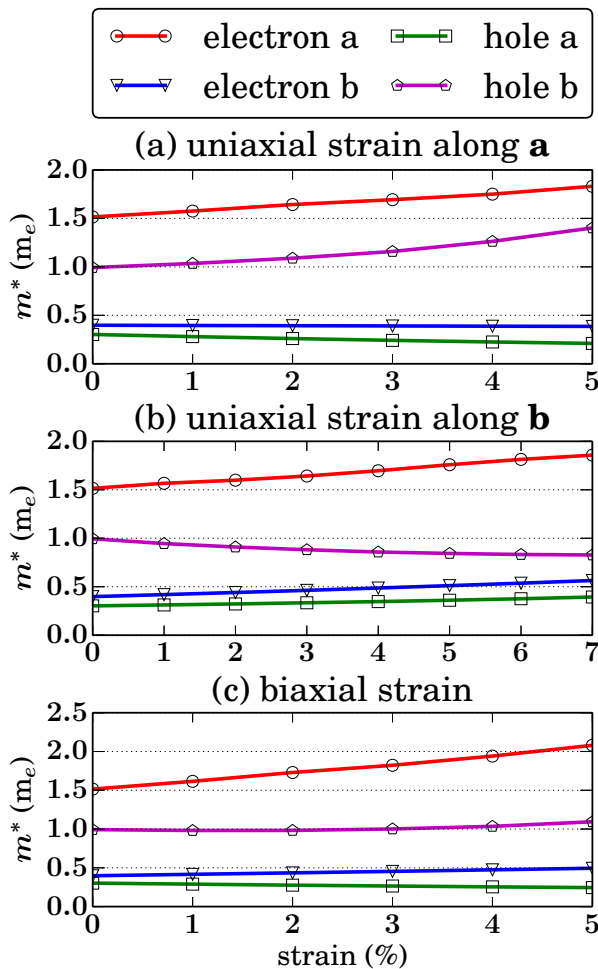


Fig. 1.23 Variation of the effective mass of electron and hole along the  $a$  and  $b$  directions at the  $\Gamma$ -point with strain.

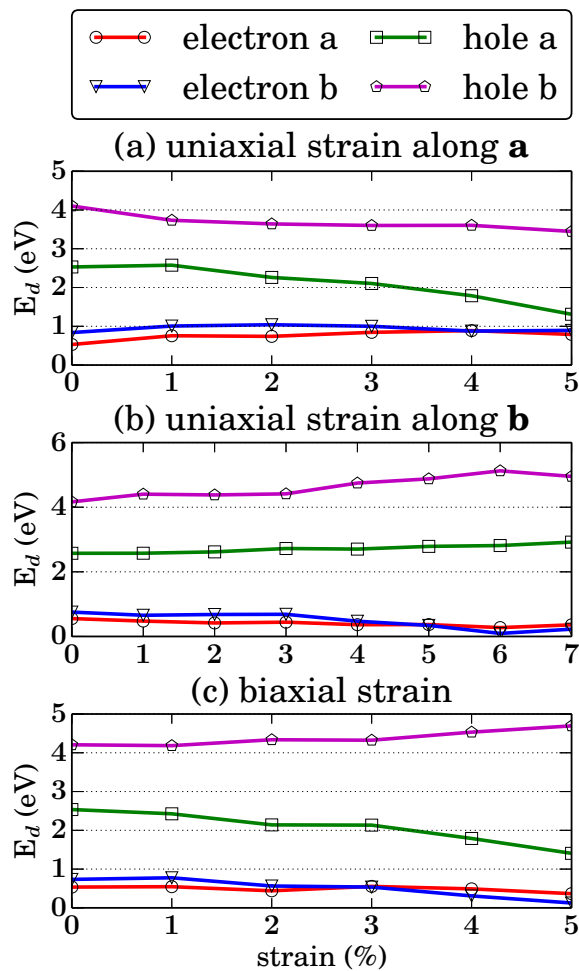


Fig. 1.24 Variation of the (a) deformation potential constant ( $E_d$ ) with strain.

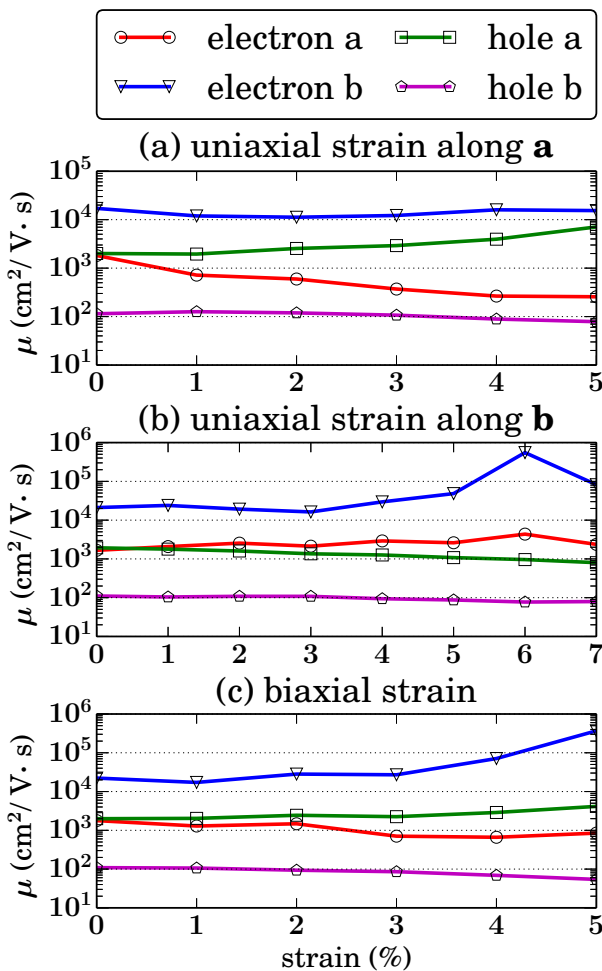


Fig. 1.25 Variation of the mobility ( $\mu$ ) with strain.

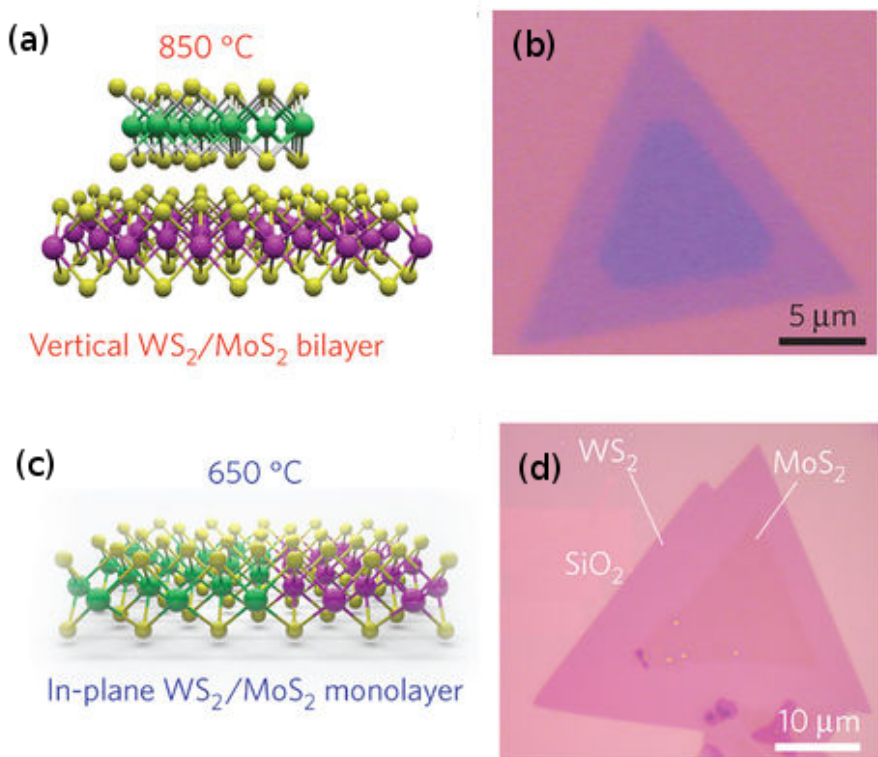


Fig. 1.26 (a) and (d) vertical and (c) and (d) lateral  $\text{WS}_2/\text{MoS}_2$  heterostructures.  
Image adapted from: [101]

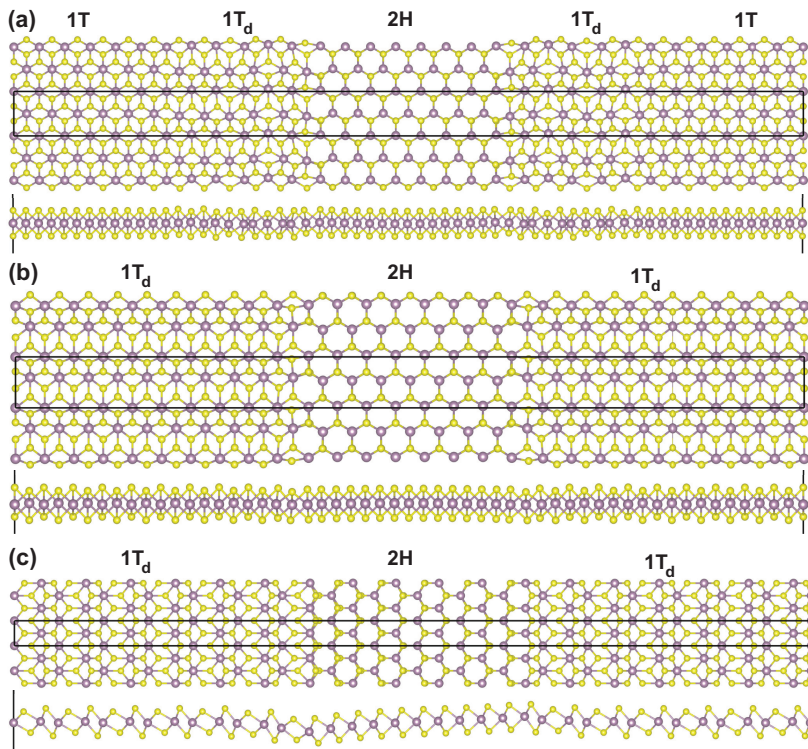


Fig. 1.27 Device models where 1H phase of MoS<sub>2</sub> is sandwiched between metallic MoS<sub>2</sub> electrodes. In (a) the  $\alpha$ -device, (b) the  $\beta$ -device, and (c) the  $\gamma$ -device. For the  $\alpha$  and  $\beta$  devices, the interfaces between metallic and semiconducting MoS<sub>2</sub> have an armchair termination while a zigzag termination in the  $\gamma$ -device.

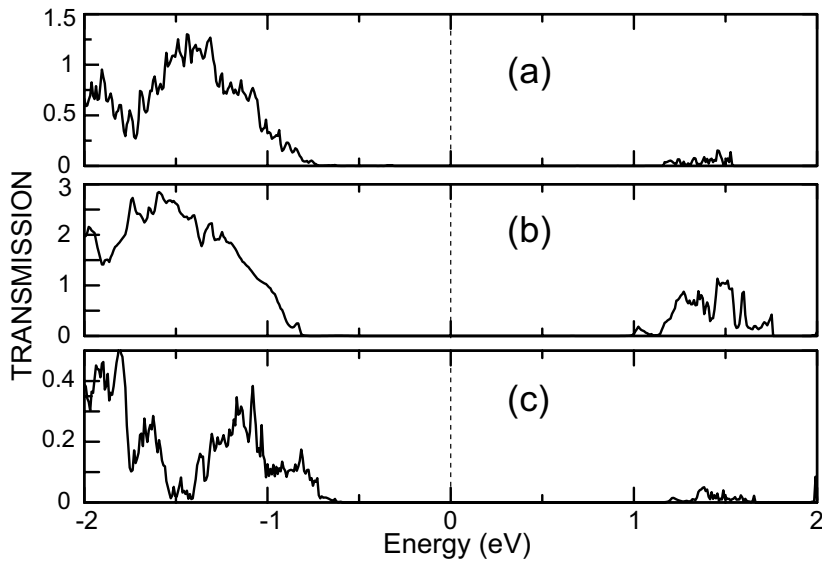


Fig. 1.28 The zero bias transmission spectra for (a) the  $\alpha$ -device, (b) the  $\beta$  device, and (c) the  $\gamma$ -device.

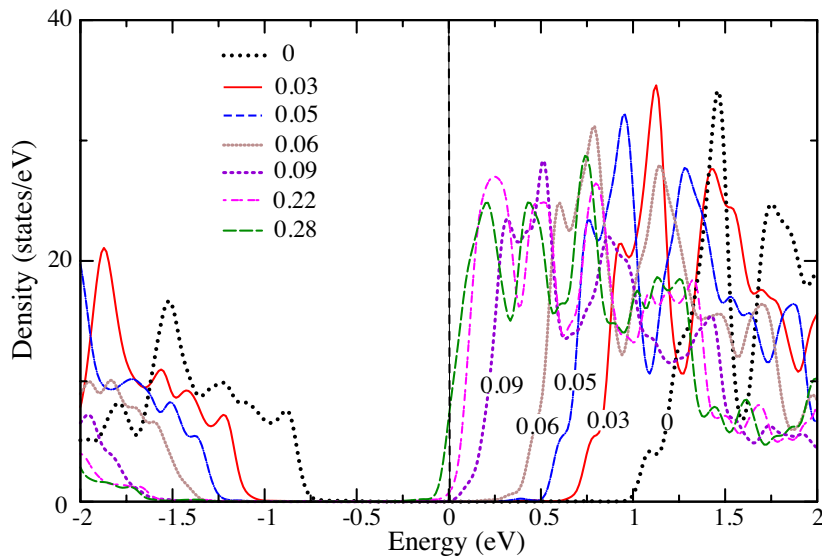


Fig. 1.29 Projected density of states of the valence and conduction band of 1H-MoS<sub>2</sub> as a function of electron concentration for the  $\beta$ -device. Here, we only show the PDOS of the central part of 1H-MoS<sub>2</sub> where the effect of the interface is minimal. The Fermi level marks the zero energy. Electron concentrations (per formula unit of 1T<sub>d</sub> phase) are given.

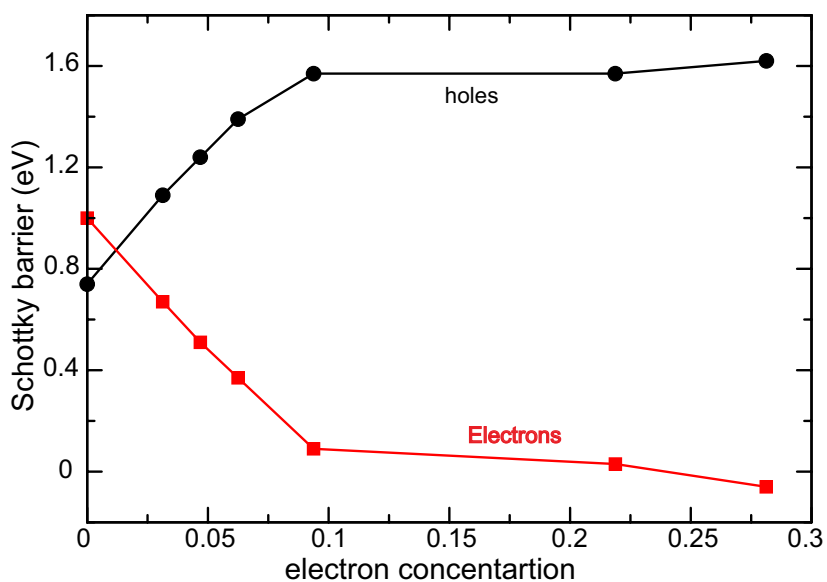


Fig. 1.30 Variation of Schottky barrier for the  $\beta$ -device as a function of electron concentration (per formula unit of  $1T_d$  part) for both electrons (red) and holes (black).

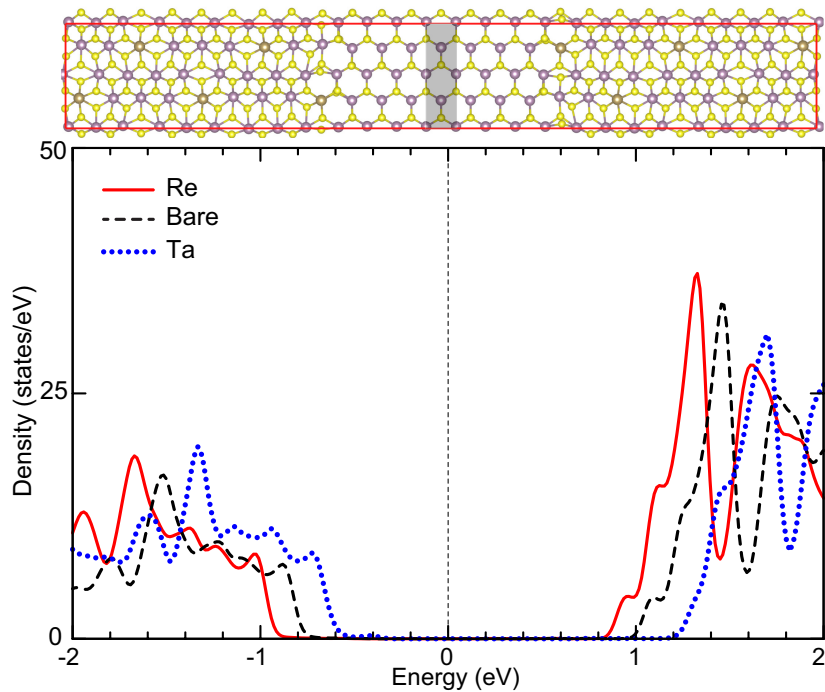


Fig. 1.31 Projected density of states of the valence and conduction band of the central part of 1H-MoS<sub>2</sub> for Re and Ta doped devices. In the top figure, gray region highlights the central part of 1H phase for which PDOS is calculated. For comparison, PDOS of bare device is also shown.

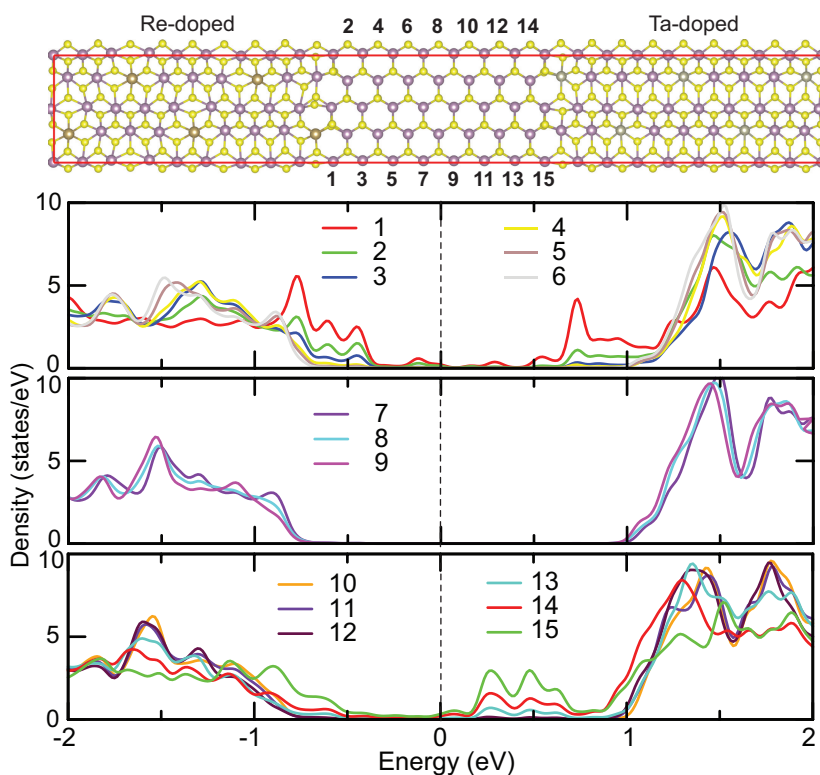


Fig. 1.32 Projected density of states of 1H-MoS<sub>2</sub> at the different position on 1H-MoS<sub>2</sub>. The Fermi level marks the zero energy.

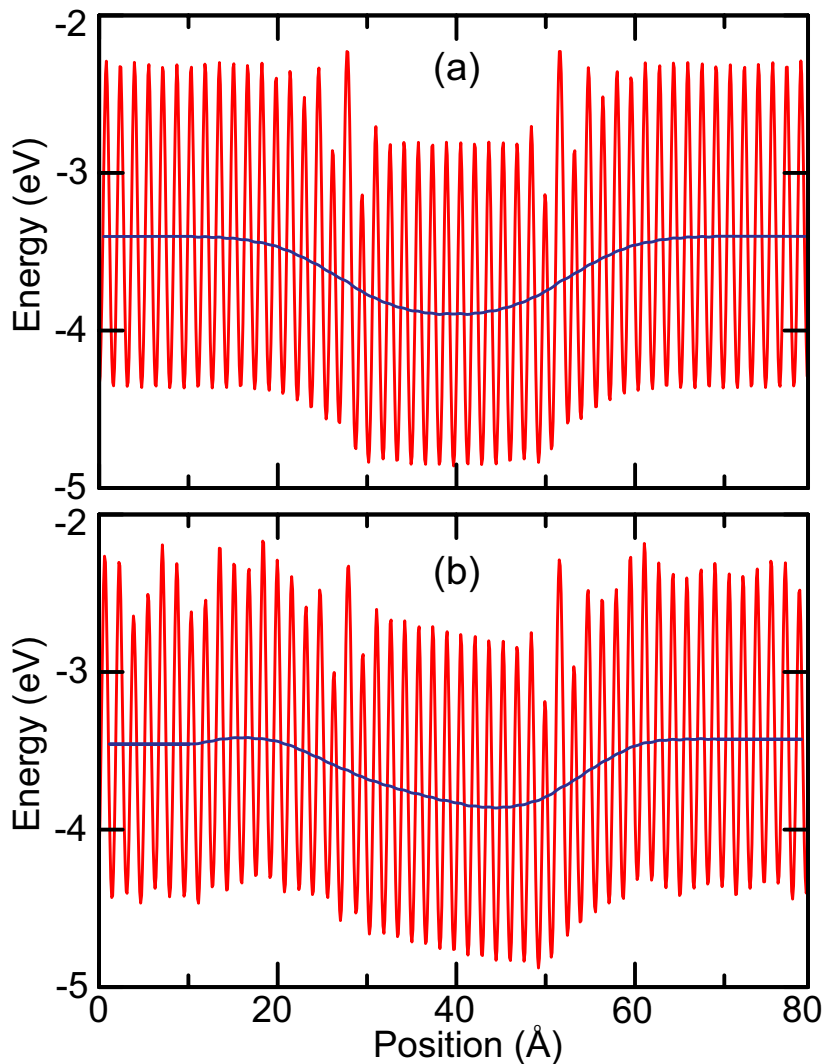


Fig. 1.33 Self-consistent electrostatic potential profile along the interface of armchair (a) pristine and (b) doped  $1T_d$ -1H- $1T_d$  MoS<sub>2</sub> heterostructure. The right (left)  $1T_d$  MoS<sub>2</sub> is doped with Re (Ta). Blue curve denotes the plane average potential along the heterostructure.



# Bibliography

- [1] R. Lieth, *Preparation and crystal growth of materials with layered structures*, Vol. 1 (Springer, 1977) (cit. on p. 2).
- [2] C. Meade, and R. Jeanloz, “Static compression of  $\text{Ca}(\text{OH})_2$  at room temperature: observations of amorphization and equation of state measurements to 10.7 GPa”, *Geophys. Res. Lett.* **17**, 1157–1160 (1990) (cit. on p. 2).
- [3] M. B. Kruger, Q. Williams, and R. Jeanloz, “Vibrational spectra of  $\text{Mg}(\text{OH})_2$  and  $\text{Ca}(\text{OH})_2$  under pressure”, *The Journal of Chemical Physics* **91**, 5910–5915 (1989) (cit. on p. 2).
- [4] J. H. Nguyen, M. B. Kruger, and R. Jeanloz, “Evidence for “partial” (sublattice) amorphization in  $\text{Co}(\text{OH})_2$ ”, *Physical Review Letters* **78**, 1936–1939 (1997) (cit. on p. 2).
- [5] S. Raugei, P. L. Silvestrelli, and M. Parrinello, “Pressure-induced frustration and disorder in  $\text{Mg}(\text{OH})_2$  and  $\text{Ca}(\text{OH})_2$ ”, *Physical Review Letters* **83**, 2222–2225 (1999) (cit. on p. 2).
- [6] T. S. Duffy, C. Meade, Y. Fei, H.-K. Mao, and R. J. Hemley, “High-pressure phase transition in brucite,  $\text{Mg}(\text{OH})_2$ ”, *Am. Mineral.* **80**, 222–230 (1995) (cit. on p. 2).
- [7] S. Ekbundit, et al., “New high-pressure phase and pressure-induced amorphization of  $\text{Ca}(\text{OH})_2$ : grain size effect”, *J. Solid State Chem.* **126**, 300–307 (1996) (cit. on p. 2).
- [8] K. Catalli, S.-H. Shim, and V. B. Prakapenka, “A crystalline-to-crystalline phase transition in  $\text{Ca}(\text{OH})_2$  at 8 GPa and room temperature”, *Geophys. Res. Lett.* **35**, L05312 (2008) (cit. on p. 2).
- [9] R. Iizuka, et al., “Pressure responses of portlandite and h-d isotope effects on pressure-induced phase transitions”, *Phys. Chem. Miner.* **38**, 777–785 (2011) (cit. on p. 2).
- [10] B. Winkler, et al., “Ab initio total energy study of brucite, diaspore and hypothetical hydrous wadsleyite”, *English, Phys. Chem. Miner.* **22**, 461–467 (1995) (cit. on p. 2).

- [11] P. Baranek, A. Lichanot, R. Orlando, and R. Dovesi, "Structural and vibrational properties of solid mg(oh)2 and ca(oh)2 – performances of various hamiltonians", *Chemical Physics Letters* **340**, 362–369 (2001) (cit. on p. 2).
- [12] K. Azuma, T. Oda, and S. Tanaka, "Vibration analysis of o-h stretching mode in mg(oh)2, ca(oh)2, lioh, and naoh by plane-wave pseudopotential DFT calculation", *Comput. Theor. Chem.* **963**, 215–220 (2011) (cit. on p. 2).
- [13] P. D'Arco, M. Causà, C. Roetti, and B. Silvi, "Periodic hartree-fock study of a weakly bonded layer structure: brucite mg(OH)2", *Physical Review B* **47**, 3522–3529 (1993) (cit. on pp. 2, 10).
- [14] A. Pishtshev, S. Z. Karazhanov, and M. Klosov, "Materials properties of magnesium and calcium hydroxides from first-principles calculations", *Computational Materials Science* **95**, 693–705 (2014) (cit. on pp. 2, 6, 7).
- [15] A. Pishtshev, S. Z. Karazhanov, and M. Klosov, "Excitons in mg(oh)2 and ca(oh)2 from ab initio calculations", *Solid State Commun.* **193**, 11–15 (2014) (cit. on p. 2).
- [16] W. Ren, and H.-M. Cheng, "The global growth of graphene", *Nature Nanotechnology* **9**, 726–730 (2014) (cit. on p. 2).
- [17] Y. Yu, et al., "Controlled scalable synthesis of uniform, high-quality mono-layer and few-layer MoS2 Films", *Scientific Reports* **3** (2013) 10 .1038 / srep01866 (cit. on p. 2).
- [18] D. Alfè, "Phon: a program to calculate phonons using the small displacement method", *Comput. Phys. Commun.* **180**, 40 YEARS OF CPC: A celebratory issue focused on quality software for high performance, grid and novel computing architectures, 2622–2633 (2009) (cit. on pp. 3, 14).
- [19] S. Grimme, "Semiempirical gga-type density functional constructed with a long-range dispersion correction", *J. Comput. Chem.* **27**, 1787–1799 (2006) (cit. on p. 3).
- [20] W. Tang, E. Sanville, and G. Henkelman, "A grid-based bader analysis algorithm without lattice bias", *J. Phys.: Condens. Matter* **21**, 084204 (2009) (cit. on pp. 4, 31).
- [21] E. Sanville, S. D. Kenny, R. Smith, and G. Henkelman, "Improved grid-based algorithm for bader charge allocation", *J. Comput. Chem.* **28**, 899–908 (2007) (cit. on pp. 4, 31).
- [22] G. Henkelman, A. Arnaldsson, and H. Jónsson, "A fast and robust algorithm for bader decomposition of charge density", *Computational Materials Science* **36**, 354–360 (2006) (cit. on pp. 4, 31).
- [23] L. Desgranges, et al., "Hydrogen thermal motion in calcium hydroxide: Ca(OH)<sub>2</sub>", *Acta Crystallographica Section B* **49**, 812–817 (1993) (cit. on p. 7).

- [24] W. R. Busing, and H. A. Levy, "Neutron diffraction study of calcium hydroxide", *The Journal of Chemical Physics* **26**, 563–568 (1957) (cit. on p. 7).
- [25] C. Ataca, M. Topsakal, E. Aktürk, and S. Ciraci, "A comparative study of lattice dynamics of three- and two-dimensional mos<sub>2</sub>", *The Journal of Physical Chemistry C* **115**, 16354–16361 (2011) (cit. on p. 7).
- [26] M. Topsakal, E. Aktürk, and S. Ciraci, "First-principles study of two- and one-dimensional honeycomb structures of boron nitride", *Phys. Rev. B* **79**, 115442 (2009) (cit. on p. 8).
- [27] Q. Peng, W. Ji, and S. De, "Mechanical properties of the hexagonal boron nitride monolayer: ab initio study", *Computational Materials Science* **56**, 11–17 (2012) (cit. on p. 8).
- [28] H. Şahin, et al., "Monolayer honeycomb structures of group-iv elements and III-V binary compounds: first-principles calculations", *Phys. Rev. B* **80**, 155453 (2009) (cit. on p. 8).
- [29] M. Posternak, A. Baldereschi, A. J. Freeman, and E. Wimmer, "Prediction of electronic surface states in layered materials: graphite", *Phys. Rev. Lett.* **52**, 863–866 (1984) (cit. on p. 12).
- [30] M. Posternak, A. Baldereschi, A. J. Freeman, E. Wimmer, and M. Weinert, "Prediction of electronic interlayer states in graphite and reinterpretation of alkali bands in graphite intercalation compounds", *Phys. Rev. Lett.* **50**, 761–764 (1983) (cit. on p. 12).
- [31] G. N. Greaves, A. L. Greer, R. S. Lakes, and T. Rouxel, "Poisson's ratio and modern materials", *Nat. Mater.* **10**, 823–837 (2011) (cit. on p. 12).
- [32] S. Baroni, S. de Gironcoli, A. Dal Corso, and P. Giannozzi, "Phonons and related crystal properties from density-functional perturbation theory", *Rev. Mod. Phys.* **73**, 515–562 (2001) (cit. on p. 14).
- [33] X.-Q. Zhang, C.-H. Lin, Y.-W. Tseng, K.-H. Huang, and Y.-H. Lee, "Synthesis of lateral heterostructures of semiconducting atomic layers", *Nano Letters* **15**, 410–415 (2015) (cit. on pp. 16, 29, 44).
- [34] Y. Ding, and Y. Wang, "Hydrogen-induced stabilization and tunable electronic structures of penta-silicene: a computational study", *J. Mater. Chem. C* **3**, 11341–11348 (2015) (cit. on pp. 16, 18).
- [35] X. Li, Y. Dai, M. Li, W. Wei, and B. Huang, "Stable si-based pentagonal monolayers: high carrier mobilities and applications in photocatalytic water splitting", *J. Mater. Chem. A* **3**, 24055–24063 (2015) (cit. on pp. 16, 18).
- [36] M. Parrinello, and A. Rahman, "Crystal structure and pair potentials: a molecular-dynamics study", *Phys. Rev. Lett.* **45**, 1196–1199 (1980) (cit. on p. 17).
- [37] M. Parrinello, and A. Rahman, "Polymorphic transitions in single crystals: a new molecular dynamics method", *J. Appl. Phys.* **52**, 7182–7190 (1981) (cit. on p. 17).

- [38] M. Allen, and D. Tildesley, *Computer simulation of liquids*, Oxford Science Publ (Clarendon Press, 1989) (cit. on p. 17).
- [39] D. Caliste, *V\_sim atomic visualization package available online*, [http://inac.cea.fr/L\\_Sim/V\\_Sim/index.en.html](http://inac.cea.fr/L_Sim/V_Sim/index.en.html) (visited on 03/25/2016) (cit. on p. 17).
- [40] Z. Wang, et al., “Electronic and optical properties of novel carbon allotropes”, *Carbon* **101**, 77–85 (2016) (cit. on p. 19).
- [41] Z. Zhao, et al., “Tetragonal allotrope of group 14 elements”, *JACS* **134**, 12362–12365 (2012) (cit. on p. 19).
- [42] K. Momma, and F. Izumi, “VESTA3 for three-dimensional visualization of crystal, volumetric and morphology data”, *J. Appl. Cryst.* **44**, 1272–1276 (2011) (cit. on p. 20).
- [43] F. Mouhat, and F.-X. Coudert, “Necessary and sufficient elastic stability conditions in various crystal systems”, *Phys. Rev. B* **90**, 224104 (2014) (cit. on p. 23).
- [44] T. Morishita, M. J. Spencer, S. P. Russo, I. K. Snook, and M. Mikami, “Surface reconstruction of ultrathin silicon nanosheets”, *Chem. Phys. Lett.* **506**, 221–225 (2011) (cit. on p. 25).
- [45] Y. Sakai, and A. Oshiyama, “Structural stability and energy-gap modulation through atomic protrusion in freestanding bilayer silicene”, *Phys. Rev. B* **91**, 201405 (2015) (cit. on p. 25).
- [46] K. S. Novoselov, et al., “Electric field effect in atomically thin carbon films”, *Science* **306**, 666–669 (2004) (cit. on p. 29).
- [47] K. S. Novoselov, et al., “Two-dimensional atomic crystals”, *Proc. Natl. Acad. Sci. U. S. A.* **102**, 10451–10453 (2005) (cit. on p. 29).
- [48] A. K. Geim, and K. S. Novoselov, “The rise of graphene”, *Nat. Mater.* **6**, 183–191 (2007) (cit. on p. 29).
- [49] B. Radisavljevic, A. Radenovic, J. Brivio, V. Giacometti, and A. Kis, “Single-layer MoS<sub>2</sub> transistors”, *Nature Nanotech.* **6**, 147–150 (2011) (cit. on p. 29).
- [50] Z. Zeng, et al., “Single-layer semiconducting nanosheets: high-yield preparation and device fabrication”, *Angew. Chem. Int. Ed.* **50**, 11093–11097 (2011) (cit. on p. 29).
- [51] C. Ataca, H. Şahin, and S. Ciraci, “Stable, single-layer mx<sub>2</sub> Transition-metal oxides and dichalcogenides in a honeycomb-like structure”, *The Journal of Physical Chemistry C* **116**, 8983–8999 (2012) (cit. on p. 29).
- [52] G.-B. Liu, D. Xiao, Y. Yao, X. Xu, and W. Yao, “Electronic structures and theoretical modelling of two-dimensional group-vib transition metal dichalcogenides”, *Chem. Soc. Rev.* **44**, 2643–2663 (2015) (cit. on p. 29).
- [53] S. Tongay, et al., “Monolayer behaviour in bulk ReS<sub>2</sub> due to electronic and vibrational decoupling”, *Nature Communications* **5** (2014) 10.1038/ncomms4252 (cit. on pp. 29, 48).

- [54] S. Horzum, et al., "Formation and stability of point defects in monolayer rhenium disulfide", *Phys. Rev. B* **89**, 155433 (2014) (cit. on p. 29).
- [55] L. Li, et al., "Black phosphorus field-effect transistors", *Nat Nano* **9**, 372–377 (2014) (cit. on p. 29).
- [56] H. Liu, et al., "Phosphorene: an unexplored 2D semiconductor with a high hole mobility", *ACS Nano* **8**, 4033–4041 (2014) (cit. on p. 29).
- [57] A. H. Woomer, et al., "Phosphorene: synthesis, scale-up, and quantitative optical spectroscopy", *ACS Nano* **9**, 8869–8884 (2015) (cit. on p. 29).
- [58] J. Guan, Z. Zhu, and D. Tománek, "Phase coexistence and metal-insulator transition in few-layer phosphorene: a computational study", *Phys. Rev. Lett.* **113**, 046804 (2014) (cit. on p. 29).
- [59] D. Çakır, C. Sevik, and F. M. Peeters, "Significant effect of stacking on the electronic and optical properties of few-layer black phosphorus", *Phys. Rev. B* **92**, 165406 (2015) (cit. on p. 29).
- [60] D. Çakır, H. Sahin, and F. M. Peeters, "Tuning of the electronic and optical properties of single-layer black phosphorus by strain", *Phys. Rev. B* **90**, 205421 (2014) (cit. on p. 29).
- [61] M. Naguib, V. N. Mochalin, M. W. Barsoum, and Y. Gogotsi, "25th anniversary article: mxenes: a new family of two-dimensional materials", *Advanced Materials* **26**, 992–1005 (2014) (cit. on p. 29).
- [62] K. F. Mak, C. Lee, J. Hone, J. Shan, and T. F. Heinz, "Atomically ThinMoS<sub>2</sub>: a new direct-gap semiconductor", *Physical Review Letters* **105** (2010) 10. 1103/physrevlett.105.136805 (cit. on p. 29).
- [63] A. A. Balandin, et al., "Superior thermal conductivity of single-layer graphene", *Nano Lett.* **8**, 902–907 (2008) (cit. on p. 29).
- [64] J. O. Island, et al., "Ultrahigh photoresponse of few-layer tis3 Nanoribbon transistors", *Advanced Optical Materials* **2**, 641–645 (2014) (cit. on p. 29).
- [65] J. O. Island, et al., "Tis3 Transistors with tailored morphology and electrical properties", *Advanced Materials* **27**, 2595–2601 (2015) (cit. on p. 29).
- [66] T. Vogelsang, and K. R. Hofmann, "Electron transport in strained si layers on si1-xGexsubstrates", *Applied Physics Letters* **63**, 186–188 (1993) (cit. on p. 29).
- [67] J. Welser, J. Hoyt, S. Takagi, and J. Gibbons, "Strain dependence of the performance enhancement in strained-si n-MOSFETs", in *Electron devices meeting, 1994. iedm '94. technical digest., international* (Dec. 1994), pp. 373–376 (cit. on p. 29).
- [68] K. Kaasbjerg, K. S. Thygesen, and K. W. Jacobsen, "Phonon-limited mobility inn-type single-layer MoS<sub>2</sub>from first principles", *Physical Review B* **85** (2012) 10.1103/physrevb.85.115317 (cit. on pp. 29, 31).

- [69] W. Zhang, Z. Huang, W. Zhang, and Y. Li, "Two-dimensional semiconductors with possible high room temperature mobility", *Nano Res.* **7**, 1731–1737 (2014) (cit. on p. 29).
- [70] Y. Cai, G. Zhang, and Y.-W. Zhang, "Polarity-reversed robust carrier mobility in monolayer mos2 Nanoribbons", *J. Am. Chem. Soc.* **136**, 6269–6275 (2014) (cit. on pp. 29, 30).
- [71] R. Fei, and L. Yang, "Strain-engineering the anisotropic electrical conductance of few-layer black phosphorus", *Nano Lett.* **14**, 2884–2889 (2014) (cit. on pp. 29, 30, 40).
- [72] H. M. Stewart, S. A. Shevlin, C. R. A. Catlow, and Z. X. Guo, "Compressive straining of bilayer phosphorene leads to extraordinary electron mobility at a new conduction band edge", *Nano Lett.* **15**, 2006–2010 (2015) (cit. on p. 29).
- [73] S. Yu, H. D. Xiong, K. Eshun, H. Yuan, and Q. Li, "Phase transition, effective mass and carrier mobility of mos2 monolayer under tensile strain", *Appl. Surf. Sci.* **325**, 27–32 (2015) (cit. on p. 29).
- [74] G. Kresse, and J. Hafner, "Ab initio molecular-dynamics simulation of the liquid-metal-amorphous-semiconductor transition in germanium", *Phys. Rev. B* **49**, 14251–14269 (1994) (cit. on pp. 30, 44).
- [75] G. Kresse, and J. Furthmüller, "Efficiency of ab-initio total energy calculations for metals and semiconductors using a plane-wave basis set", *Computational Materials Science* **6**, 15–50 (1996) (cit. on pp. 30, 44).
- [76] G. Kresse, and J. Furthmüller, "Efficiency of ab-initio total energy calculations for metals and semiconductors using a plane-wave basis set", *Comput. Mater. Sci.* **6**, 15–50 (1996) (cit. on pp. 30, 44).
- [77] G. Kresse, and J. Furthmüller, "Efficient iterative schemes for ab initio total-energy calculations using a plane-wave basis set", *Phys. Rev. B* **54**, 11169–11186 (1996) (cit. on pp. 30, 44).
- [78] P. E. Blöchl, "Projector augmented-wave method", *Phys. Rev. B* **50**, 17953–17979 (1994) (cit. on pp. 30, 44).
- [79] G. Kresse, and D. Joubert, "From ultrasoft pseudopotentials to the projector augmented-wave method", *Phys. Rev. B* **59**, 1758–1775 (1999) (cit. on pp. 30, 44).
- [80] J. P. Perdew, K. Burke, and M. Ernzerhof, "Generalized gradient approximation made simple", *Phys. Rev. Lett.* **77**, 3865–3868 (1996) (cit. on pp. 30, 44).
- [81] J. P. Perdew, K. Burke, and M. Ernzerhof, "Generalized gradient approximation made simple [phys. rev. lett. 77, 3865 (1996)]", *Phys. Rev. Lett.* **78**, 1396–1396 (1997) (cit. on pp. 30, 44).

- [82] M.-Q. Long, L. Tang, D. Wang, L. Wang, and Z. Shuai, “Theoretical predictions of size-dependent carrier mobility and polarity in graphene”, *J. Am. Chem. Soc.* **131**, 17728–17729 (2009) (cit. on p. 30).
- [83] A. Togo, and I. Tanaka, “First principles phonon calculations in materials science”, *Scr. Mater.* **108**, 1–5 (2015) (cit. on p. 30).
- [84] J. Bardeen, and W. Shockley, “Deformation potentials and mobilities in non-polar crystals”, *Phys. Rev.* **80**, 72–80 (1950) (cit. on p. 30).
- [85] J. Xi, M. Long, L. Tang, D. Wang, and Z. Shuai, “First-principles prediction of charge mobility in carbon and organic nanomaterials”, *Nanoscale* **4**, 4348 (2012) (cit. on p. 30).
- [86] J. Qiao, X. Kong, Z.-X. Hu, F. Yang, and W. Ji, “High-mobility transport anisotropy and linear dichroism in few-layer black phosphorus”, *Nat. Commun.* **5**, 4475 (2014) (cit. on p. 30).
- [87] J. Dai, and X. C. Zeng, “Titanium trisulfide monolayer: theoretical prediction of a new direct-gap semiconductor with high and anisotropic carrier mobility”, *Angewandte Chemie International Edition* **54**, 7572–7576 (2015) (cit. on pp. 30–32, 34).
- [88] J. Kang, H. Sahin, H. D. Ozaydin, R. T. Senger, and F. M. Peeters, “TiS<sub>3</sub>nanoribbons: width-independent band gap and strain-tunable electronic properties”, *Physical Review B* **92** (2015) 10.1103/physrevb.92.075413 (cit. on p. 30).
- [89] M. Yu, and D. R. Trinkle, “Accurate and efficient algorithm for bader charge integration”, *The Journal of Chemical Physics* **134**, 064111 (2011) (cit. on p. 31).
- [90] D. W. Oxtoby, H. P. Gillis, and A. Campion, *Principles of modern chemistry*, 7th ed. (Brooks Cole, May 2011) (cit. on p. 32).
- [91] J. Kang, H. Sahin, and F. M. Peeters, “Mechanical properties of monolayer sulphides: a comparative study between mos<sub>2</sub>, hfs<sub>2</sub> and tis<sub>3</sub>”, *Phys. Chem. Chem. Phys.* **17**, 27742–27749 (2015) (cit. on p. 34).
- [92] D. Çakır, F. M. Peeters, and C. Sevik, “Mechanical and thermal properties of h-mx<sub>2</sub> (m=cr, mo, w; x=o, s, se, te) monolayers: a comparative study”, *Appl. Phys. Lett.* **104**, 203110 (2014) (cit. on p. 34).
- [93] G. Q. Huang, and Z. W. Xing, “Band-gap tunability and dynamical instability in strained monolayer and bilayer phosphorenes”, *J. Phys.: Condens. Matter* **27**, 175006 (2015) (cit. on p. 37).
- [94] R. Biele, et al., “Strain-induced band gap engineering in layered tis<sub>3</sub>”, *Nano Research* (2017) 10.1007/s12274-017-1622-3 (cit. on pp. 38, 39).
- [95] M. Li, J. Dai, and X. C. Zeng, “Tuning the electronic properties of transition-metal trichalcogenides via tensile strain”, *Nanoscale* **7**, 15385–15391 (2015) (cit. on p. 38).
- [96] A. K. Geim, and I. V. Grigorieva, “Van der waals heterostructures”, *Nature* **499**, 419–425 (2013) (cit. on p. 42).

- [97] Y. Liu, et al., “Van der Waals heterostructures and devices”, *Nat. Rev. Mater.* **1**, 16042 (2016) (cit. on p. 42).
- [98] E. Pomerantseva, and Y. Gogotsi, “Two-dimensional heterostructures for energy storage”, *Nat. Energy* **2**, 17089 (2017) (cit. on p. 42).
- [99] D. Jena, K. Banerjee, and G. H. Xing, “2D crystal semiconductors: Intimate contacts”, *Nat. Mater.* **13**, 1076–1078 (2014) (cit. on p. 42).
- [100] M. Chhowalla, D. Voiry, J. Yang, H. S. Shin, and K. P. Loh, “Phase-engineered transition-metal dichalcogenides for energy and electronics”, *MRS Bulletin* **40**, 585–591 (2015) (cit. on p. 42).
- [101] Y. Gong, et al., “Vertical and in-plane heterostructures from WS<sub>2</sub>/MoS<sub>2</sub> monolayers”, *Nature Materials* **13**, 1135–1142 (2014) (cit. on p. 55).
- [102] J. Singh, *Physics of semiconductors and their heterostructures*, Electrical engineering series (McGraw-Hill, 1993) (cit. on p. 43).
- [103] G. Agostini, and C. Lamberti, *Characterization of semiconductor heterostructures and nanostructures* (Elsevier Science, 2011) (cit. on p. 43).
- [104] L.-Y. Gan, Q. Zhang, Y. Cheng, and U. Schwingenschlögl, “Two-dimensional ferromagnet/semiconductor transition metal dichalcogenide contacts: *p*-type Schottky barrier and spin-injection control”, *Phys. Rev. B* **88**, 235310 (2013) (cit. on p. 43).
- [105] N. Wu, et al., “Collective electronic behaviors of laterally heterostructured armchair mos<sub>2</sub>-Nbs<sub>2</sub> nanoribbons”, *Journal of Applied Physics* **118**, 084306 (2015) (cit. on p. 43).
- [106] A. Di Bartolomeo, “Graphene Schottky diodes: an experimental review of the rectifying graphene/semiconductor heterojunction”, *Physics Reports* **606**, 1–58 (2016) (cit. on p. 43).
- [107] K.-A. N. Duerloo, and E. J. Reed, “Structural phase transitions by design in monolayer alloys”, *ACS Nano* **10**, 289–297 (2016) (cit. on p. 43).
- [108] A. Allain, J. Kang, K. Banerjee, and A. Kis, “Electrical contacts to two-dimensional semiconductors”, *Nat. Mater.* **14**, 1195–1205 (2015) (cit. on p. 43).
- [109] Y. Matsuda, W.-Q. Deng, and W. A. Goddard, “Contact resistance for “end-contacted” metal-graphene and metal-nanotube interfaces from quantum mechanics”, *The Journal of Physical Chemistry C* **114**, 17845–17850 (2010) (cit. on p. 43).
- [110] J. Kang, W. Liu, D. Sarkar, D. Jena, and K. Banerjee, “Computational study of metal contacts to monolayer transition-metal dichalcogenide semiconductors”, *Phys. Rev. X* **4**, 031005 (2014) (cit. on p. 43).
- [111] G. Eda, et al., “Coherent atomic and electronic heterostructures of single-layer mos<sub>2</sub>”, *ACS Nano* **6**, 7311–7317 (2012) (cit. on pp. 43, 44, 46).

- [112] R. Kappera, et al., "Phase-engineered low-resistance contacts for ultra-thin MoS<sub>2</sub> transistors", *Nature Materials* **13**, 1128–1134 (2014) (cit. on p. 44).
- [113] X. Fan, et al., "Fast and efficient preparation of exfoliated 2H mos<sub>2</sub> Nanosheets by sonication-assisted lithium intercalation and infrared laser-induced 1T to 2H phase reversion", *Nano Letters* **15**, 5956–5960 (2015) (cit. on p. 44).
- [114] C. Huang, et al., "Lateral heterojunctions within monolayer MoSe<sub>2</sub>–WSe<sub>2</sub> semiconductors", *Nature Materials* **13**, 1096–1101 (2014) (cit. on p. 44).
- [115] Z. Bai, T. Markussen, and K. S. Thygesen, "Electron transport across a metal/mos<sub>2</sub> interface: dependence on contact area and binding distance", *arXiv*, 1–7 (2013) (cit. on p. 44).
- [116] Z. Hu, et al., "Modulating the phase transition between metallic and semiconducting single-layer mos<sub>2</sub> and ws<sub>2</sub> through size effects", *Phys. Chem. Chem. Phys.* **17**, 1099–1105 (2015) (cit. on p. 44).
- [117] G. Sivaraman, et al., "Electronic transport along hybrid MoS<sub>2</sub> monolayers", *The Journal of Physical Chemistry C* **120**, 23389–23396 (2016) (cit. on p. 44).
- [118] M. Brandbyge, J.-L. Mozos, P. Ordejón, J. Taylor, and K. Stokbro, "Density-functional method for nonequilibrium electron transport", *Phys. Rev. B* **65**, 165401 (2002) (cit. on p. 45).
- [119] J. M. Soler, et al., "The siesta method for ab initio order- n materials simulation", *Journal of Physics: Condensed Matter* **14**, 2745 (2002) (cit. on p. 45).
- [120] N. Troullier, and J. L. Martins, "Efficient pseudopotentials for plane-wave calculations", *Phys. Rev. B* **43**, 1993–2006 (1991) (cit. on p. 45).
- [121] F. Ma, et al., "Predicting a new phase (t[prime or minute][prime or minute]) of two-dimensional transition metal di-chalcogenides and strain-controlled topological phase transition", *Nanoscale* **8**, 4969–4975 (2016) (cit. on p. 46).
- [122] B. Radisavljevic, A. Radenovic, J. Brivio, V. Giacometti, and A. Kis, "Single-layer mos<sub>2</sub> transistors", *Nature Nanotechnology* **6**, 147–150 (2011) (cit. on p. 47).
- [123] Y.-C. Lin, et al., "Single-layer res<sub>2</sub>: two-dimensional semiconductor with tunable in-plane anisotropy", *ACS Nano* **9**, 11249–11257 (2015) (cit. on p. 47).
- [124] M. Kan, et al., "Structures and phase transition of a mos<sub>2</sub> monolayer", *The Journal of Physical Chemistry C* **118**, 1515–1522 (2014) (cit. on p. 48).
- [125] Y. Katagiri, et al., "Gate-tunable atomically thin lateral mos<sub>2</sub> Schottky junction patterned by electron beam", *Nano Letters* **16**, 3788–3794 (2016) (cit. on p. 48).
- [126] A. Nourbakhsh, et al., "Mos<sub>2</sub> Field-effect transistor with sub-10 nm channel length", *Nano Letters* **16**, 7798–7806 (2016) (cit. on p. 48).

- [127] Q. Tang, and D.-e. Jiang, "Stabilization and band-gap tuning of the 1T-mos<sub>2</sub> monolayer by covalent functionalization", *Chemistry of Materials* **27**, 3743–3748 (2015) (cit. on p. 48).
- [128] D. Cakir, H. Sahin, and F. M. Peeters, "Doping of rhenium disulfide monolayers: a systematic first principles study", *Phys. Chem. Chem. Phys.* **16**, 16771–16779 (2014) (cit. on p. 48).
- [129] F. Raffone, C. Ataca, J. C. Grossman, and G. Cicero, "Mos<sub>2</sub> enhanced t-phase stabilization and tunability through alloying", *The Journal of Physical Chemistry Letters* **7**, 2304–2309 (2016) (cit. on p. 48).
- [130] T. L. Tan, M.-F. Ng, and G. Eda, "Stable monolayer transition metal dichalcogenide ordered alloys with tunable electronic properties", *The Journal of Physical Chemistry C* **120**, 2501–2508 (2016) (cit. on p. 49).
- [131] Z. Cao, M. Harb, S. Lardhi, and L. Cavallo, "Impact of interfacial defects on the properties of monolayer transition metal dichalcogenide lateral heterojunctions", *The Journal of Physical Chemistry Letters*, 1664–1669 (cit. on p. 50).

# List of Publications

## Published

- [P1] Y. Aierken, et al., “Portlandite crystal: bulk, bilayer, and monolayer structures”, Phys. Rev. B **91**, 245413 (2015) (cit. on p. 1).
- [P2] Y. Aierken, O. Leenaerts, and F. M. Peeters, “A first-principles study of stable few-layer penta-silicene”, Phys. Chem. Chem. Phys. **18**, 18486–18492 (2016) (cit. on p. 16).
- [P3] Y. Aierken, D. Çakır, and F. M. Peeters, “Strain enhancement of acoustic phonon limited mobility in monolayer tis3”, Phys. Chem. Chem. Phys. **18**, 14434–14441 (2016) (cit. on p. 29).
- [P4] Y. Aierken, O. Leenaerts, and F. M. Peeters, “Defect-induced faceted blue phosphorene nanotubes”, Phys. Rev. B **92**, 104104 (2015) (cit. on p. 51).

## Under Review

- [P5] Y. Aierken, C. Sevik, O. Gülsen, F. M. Peeters, and D. Çakır, “In pursuit of barrierless transition metal dichalcogenides lateral heterojunctions”, submitted to PRB (cit. on p. 43).